

## Lithospheric structuration onshore-offshore of the Sergipe-Alagoas passive margin, NE Brazil, based on wide-angle seismic data <sup>☆</sup>

Pinheiro Joao Marcelo <sup>1,\*</sup>, Schnurle Philippe <sup>1</sup>, Evain Mikael <sup>1</sup>, Afilhado A. <sup>2</sup>, Gallais Flora <sup>1</sup>, Klingelhofer Frauke <sup>1</sup>, Loureiro Afonso <sup>3</sup>, Fuck R. <sup>4</sup>, Soares J. <sup>4</sup>, Cupertino J.A. <sup>5</sup>, Viana A. <sup>5</sup>, Rabineau Marina <sup>6</sup>, Baltzer Agnes <sup>7</sup>, Benabdellouahed Massinissa <sup>6</sup>, Dias N. <sup>2,3</sup>, Moulin Maryline <sup>1</sup>, Aslanian Daniel <sup>1</sup>, Morvan Laetitia <sup>8</sup>, Mazé Jean-Pierre <sup>8</sup>, Pierre Delphine <sup>8</sup>, Roudaut-Pitel M. <sup>8</sup>, Rio I. <sup>9</sup>, Alves D. <sup>9</sup>, Barros Junior P. <sup>11</sup>, Biari Youssef <sup>8</sup>, Corela C. <sup>9</sup>, Crozon Jacques <sup>8</sup>, Duarte J.L. <sup>9</sup>, Ducatel Cecile <sup>8</sup>, Falcão C. <sup>11</sup>, Fernagu Philippe <sup>8</sup>, Le Piver David <sup>8</sup>, Mokeddem Zohra <sup>10</sup>, Pelleau Pascal <sup>8</sup>, Rigoti C. <sup>11</sup>, Roest Walter <sup>8</sup>, Roudaut Mickael <sup>8</sup>

<sup>1</sup> Institut Français de Recherche pour l'Exploitation de la MER, IFREMER, REM/GM, Centre de Brest, 29280, Plouzané, France

<sup>2</sup> Instituto Superior de Engenharia de Lisboa, ISEL, Instituto Politécnico de Lisboa, R. Conselheiro Emídio Navarro, 1959-007, Lisbon, Portugal

<sup>3</sup> Instituto Dom Luiz, Faculdade de Ciências, Universidade de Lisboa, Campo Grande, Ed. C1, Piso 1, 1749-016, Lisbon, Portugal

<sup>4</sup> Instituto de Geociências, Universidade de Brasília, Campus Darcy Ribeiro, 70910-900, Brasilia, Brazil

<sup>5</sup> Petrobras, Cenpes Research Center, Rio de Janeiro, Brazil

<sup>6</sup> Laboratoire Géosciences Océan, UMR6538, Université de Bretagne Occidentale, Place Nicolas Copernic, 29280, Plouzané, France

<sup>7</sup> Géolittomer, LETG UMR 6554-CNRS, Institut de Géographie et d'Aménagement Régional de l'Université de Nantes, Campus Tertre, BP 81227, 44312, Nantes, CEDEX 3, France

<sup>8</sup> Institut Français de Recherche pour l'Exploitation de la MER, IFREMER, REM/GM, Centre de Brest, 29280, Plouzané, France

<sup>9</sup> Instituto Dom Luiz, Faculdade de Ciências, Universidade de Lisboa, Campo Grande, Ed. C1, Piso 1, 1749-016, Lisbon, Portugal

<sup>10</sup> Laboratoire Géosciences Océan, UMR6538, Université de Bretagne Occidentale, Place Nicolas Copernic, 29280, Plouzané, France

<sup>11</sup> Géolittomer, LETG UMR 6554-CNRS, Institut de Géographie et d'Aménagement Régional de l'Université de Nantes, Campus Tertre, BP 81227, 44312, Nantes, CEDEX 3, France

\* Corresponding author : Joao Marcelo Pinheiro, email address : [jmpgeo@gmail.com](mailto:jmpgeo@gmail.com)

### Abstract :

The structure and nature of the crust underlying the Camamu-Almada-Jequitinhonha-Sergipe-Alagoas basins System, in the NE Brazilian margin, were investigated based on the interpretation of 12 wide-

---

angle seismic profiles acquired during the SALSA (Sergipe ALagoas Seismic Acquisition) experiment in 2014. In this work, we present two 220-km-long NW-SE combined wide-angle and reflection seismic profiles, SL 01 and SL 02, that have been acquired using 15 ocean-bottom-seismometers along each profile, offshore the southern part of the Sergipe Alagoas Basin (SAB), north of the Vaza-Barris Transfer zone. The SL 02 has a 150-km long inland continuation with 20 land-seismic-stations until the Sergipano Fold Belt (SFB). Wide-angle seismic forward modeling allows us to precisely divide the crust in three domains: beneath the continental shelf, a ~100 km wide necking zone is imaged where the continental crust thins from ~35 km on the Unthinned Continental Domain, which displays a three-layered crust structure, to less than 8 km on the Oceanic Crust Domain. In the necking zone, the upper and the middle layers thin dramatically and almost disappear, while the Moho discontinuity shows clear PmPs. The Continental-Oceanic Crust Boundary (COB) is located at ~80 km from the coastline and is marked by intracrustal seismic reflectors and changes in the seismic velocity, showing a sharp transition. On profile SL02, the oceanic crust is perturbed by a volcanic edifice together with an anomalous velocity zone underneath the area.

### Highlights

► Sergipe Alagoas Basin passive margin modeling. ► Wide-angle refraction seismic integrated with Multi-Channel reflection seismic data. ► Location of the Continental- Oceanic crust boundary. ► Lithospheric structuration and segmentation of Brazil's margin in Central Atlantic.

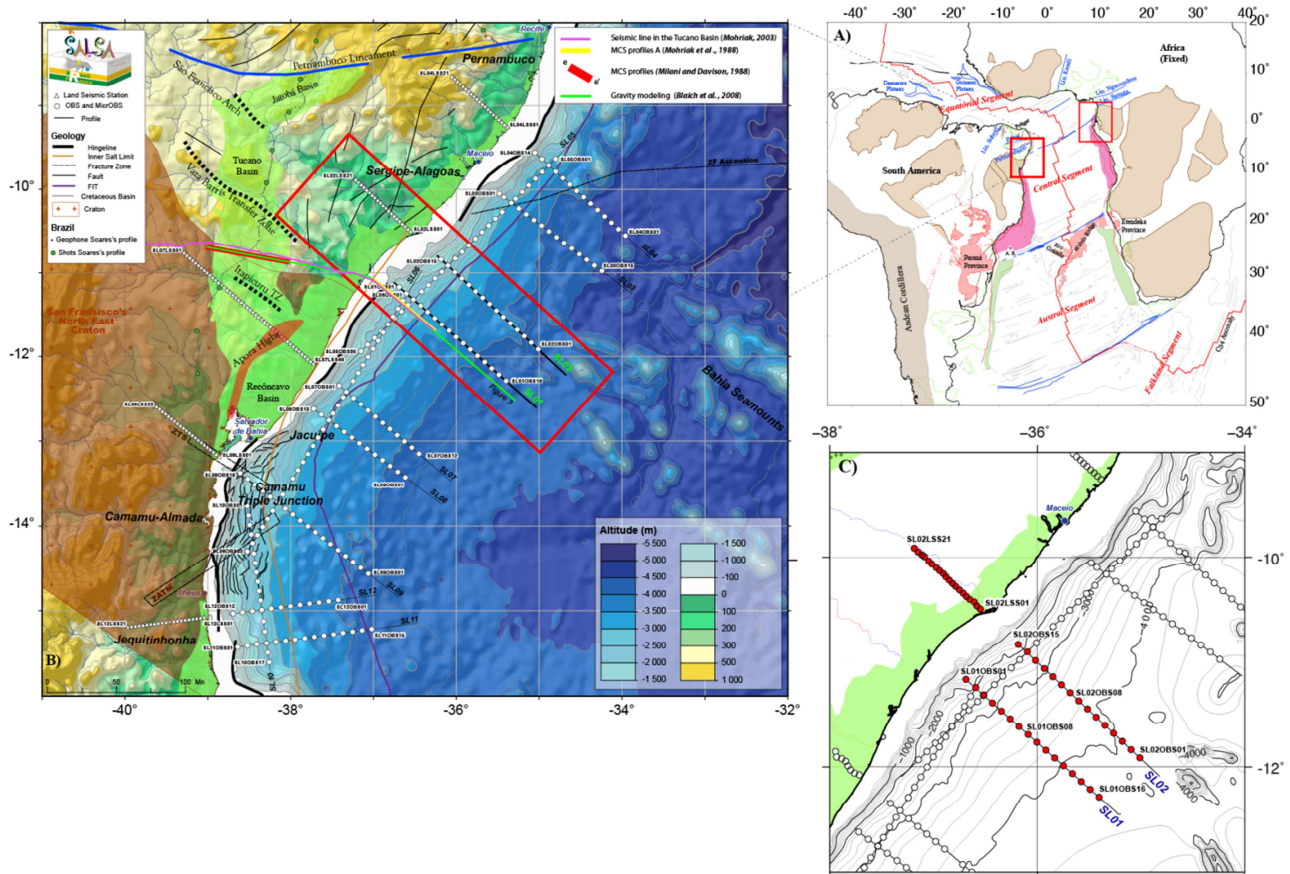
**Keywords** : South Atlantic Ocean, NE Brazil, Sergipe-Alagoas Basin, Passive Margins, Wide-angle refraction seismics, Crustal structure, Tectonic Inheritance.

★ We would like to thank two anonymous reviewers and the editor Dr. F. Audemard, who helped to improve significantly this manuscript.

## 41 Introduction

42 Understanding the processes that led to the breakup of West Gondwana (Figure 1A) and the  
43 formation of the south Atlantic Margins are still not fully achieved. The North – East Brazilian  
44 margins, which are very segmented margins, in various structural and inheritance contexts, where  
45 the aborted Recôncavo - Tucano - Jatoba rift system connects with the NS Jequitinhonha -  
46 Camamu-Almada and NE-SW Jacuípe - Sergipe-Alagoas rift systems are a strategic area to study  
47 the influence of the tectonic inheritance on margin's formation. The connection between the three  
48 system forms the Camamu triple junction. The SALSA experiment, conducted in 2014 by the  
49 Department of Marine Geosciences (IFREMER: Institut Français de Recherche pour l'Exploitation  
50 de la MER, France) and PETROBRAS (Brazil), in collaboration with the Laboratory of Oceanic  
51 Domain (IUEM: Institut Universitaire et Européen de la Mer, France), the Faculdade de Ciências da  
52 Universidade de Lisboa (IDL, Portugal) and the Universidade de Brasilia (Brazil), is aimed at  
53 constraining the crustal structure, the segmentation and the geodynamical setting of the  
54 Jequitinhonha-Almada-Camamu-Jacuípe-Alagoas-Sergipe margin segments.

55 In the year 2000's high quality seismic profiles from ION-GXT were acquired off Brazil's coast,  
56 and a few of these profiles have been published, particularly in the Brazilian southeastern margin  
57 (e.g., Henry *et al.*, 2009; Kumar *et al.*, 2012). The location of the SALSA profiles follows the  
58 location of some of the ION-GXT profiles. Seismic shots, Multi-Channel Seismic (MCS)  
59 acquisition and Ocean Bottom Seismometers (OBS) deployments were performed by the French  
60 R/V L'Atalante (IFREMER) along twelve profiles (Figure 1B). Among them, five were extended  
61 onshore by Land Seismic Stations (LSS). Here, we present the results on P-wave velocity models,  
62 based on the combined interpretation of multi-channel and wide-angle seismic data, of two profiles  
63 imaging the Sergipe-Alagoas basin (SAB), located in the northern part of the experiment, north to  
64 the Vaza-Barris transfer zone (Figures 1C and 2). The remaining basins studied during the SALSA  
65 project (Camamu (Loureiro *et al.*, 2018), Jacuípe, Tucano and Sergipe-Alagoas basins) will be  
66 discussed in companion papers.



68 Figure 1: Location of profiles of the SALSA experiment: A) General reconstruction map at Chron C34 of studied area  
 69 and conjugate margin (Moulin *et al.*, 2010). B) Bathymetry and topography on land (IHO-IOC GEBCO, 2014). Ocean  
 70 Bottom Seismometers (OBSs) are marked by white dots, MCS profiles by thick black lines, land-stations by white  
 71 triangles. The SL01 and SL02 profiles are highlighted by red rectangle. The color lines represent the location of  
 72 profiles already published in this area. Dashed black line denotes main transfer zones (Blaich *et al.*, 2008). Green area  
 73 indicates the Recôncavo-Tucano-Jatoba (RTJ) basins (Bizzi *et al.*, 2003). Brown area indicates the limits of the Sao  
 74 Francisco Craton, adapted from Hasui (2012). TMAZ: Taipus-Mirim Accommodation Zone. Note that Bahia Seamounts  
 75 are characterized by an elongated NW-SE direction. C) Bathymetry (IHO-IOC GEBCO, 2014) around the profiles  
 76 discussed in the present paper.  
 77

## 78 Geological Setting

79 Whilst in Albian time the central part of the South Atlantic presented the first oceanic crust, the  
 80 Equatorial Atlantic Ocean was only starting to open, as the last stage of the breakup of the Atlantic  
 81 Ocean, allowing the definitive water connection between the Central Atlantic and the South Atlantic  
 82 oceans (Moulin *et al.*, 2010). From the Potiguar Basin to the north to the Camamu triple junction to  
 83 the south (figure 1A), this area represents a buffer zone between these two different geodynamical  
 84 settings (Conceição and Zalan, 1998; Moulin *et al.*, 2010).

85 This buffer zone is characterized by a SW-NE elongated margin, oblique respect to the main  
 86 direction of the Fracture zones of the central segment of the South Atlantic Ocean. Onshore the  
 87 presence of a failed N-S and E-W rift: the Recôncavo-Tucano-Jatoba rift, marks the limit of the  
 88 Triangle-shaped Tucano Microplate, which rotated counterclockwise (Szatmari *et al.*, 1999; Moulin  
 89 *et al.*, 2010) during the South Atlantic opening. The Sergipe Alagoas Basin (SAB) is situated in the

90 middle of the eastern branch of this triangle, to the north of the Vaza-Barris Fault, which marks the  
91 boundary between the Sergipe basin and Jacuibe basin depocenters. It is in the east of the Sergipano  
92 Fold Belt (SFB) and south of the Pernambuco lineament, which are geological structures associated  
93 with the tectonic development of NE Brazil (Figure 2), inherited from the Neoproterozoic  
94 Brasiliano Orogeny (Davison *et al.*, 1995). The role of the Vaza-Barris transfer zone, is not yet  
95 completely understood, but it plays a significant role in the actual framework of the Brazilian  
96 margin, as it divides the Tucano basin and produces a flip in the location of its depocenters.  
97 Stratigraphically, the SAB is one of the few basins that presents Paleozoic to Jurassic/Early  
98 Cretaceous pre-rift sequences related to intracratonic subsidence and is the northern limit of the  
99 evaporite deposits (Cainelli and Mohriak, 1998).

100 Sediments in the SAB lie over the Proterozoic SFB (Figure 2). The SFB is located between the  
101 Pernambuco-Alagoas Massif and the São Francisco Craton (SFC) (Figures 1 and 2) with a  
102 triangular shape narrowing towards the west (Figure 2). The geological history of the SFB has been  
103 the subject of numerous studies (e.g. Almeida *et al.*, 1977; Davison and Santos, 1989; D'el-Rey  
104 Silva, 1999). Recently Oliveira *et al.* (2010), based on U–Pb SHRIMP (Sensitive High-Resolution  
105 Ion Microprobe) and detrital zircons ages from Carvalho *et al.* (2005), proposed that the evolution  
106 of the Sergipano Belt began with the breakup of a Palaeoproterozoic continent followed by  
107 development of a Mesoproterozoic (~980–960 Ma) continental arc possibly on the margin of the  
108 Palaeoproterozoic Pernambuco-Alagoas Massif. The extension of this continental block resulted in  
109 a stretched margin, a passive margin on the southern edge of the Pernambuco-Alagoas Massif with  
110 a rift in between. A second passive margin was formed on the São Francisco Craton. Convergence  
111 of the Pernambuco-Alagoas Massif and the São Francisco Craton led to deformation in shelf  
112 sediments, build-up of a continental arc between 630 Ma and 620 Ma, and subsequent exhumation  
113 and erosion of the Pernambuco-Alagoas Block, led to deposition of the uppermost Pre-Cambrian  
114 clastic sediments (Oliveira *et al.*, 2010).

115 The SAB presents a complete rift stratigraphic record (Mohriak, 2003). The initial rift deposits  
116 records can be observed in the onshore part of the SAB. Gomes (2005), using well logs information  
117 with seismic data (Cainelli, 1992), had tracked continuous seismic horizons related to the base of  
118 the Calumbi Formation, which marks the beginning of the drift phase. Campos Neto *et al.* (2007)  
119 elaborated the Petrobras stratigraphic chart, following the lithostratigraphic classification proposed  
120 by Schaller (1970) and Feijó (1994).

121 Mohriak *et al.* (1995, 1998, 2000) and Mohriak (2003) interpreted the regional seismic section 238-  
122 RL-343 (Figures 1 and 3). This profile is perpendicular to the coast and hinge line and extends for  
123 about 110 km from the platform to the deep water-region of the SAB. He did an interpretation

124 stratigraphically calibrated by exploration boreholes and structurally constrained by gravity  
125 modelling. The results of a deep geoseismic transect were also used by Blaich *et al.* (2008, 2011) to  
126 model the crust of the SAB in combination of new gravity data. From these past studies, we can  
127 assume some key elements:

128 • Mohriak *et al.* (1998) described a conspicuous array of strong undulated reflectors in the  
129 lower portion of the profile (Figure 3) forming an anticlinal structure that rises from the  
130 westernmost portion of the profile until the apex near the shelf-break and extends as a band of  
131 reflectors throughout most of the profile (Figure 3), from slope to deep basin. He suggested that  
132 they might correspond to intracrustal horizons that probably mark the transition from the lower  
133 crust to the upper mantle ultramafic rocks (Kemplerer *et al.*, 1986).

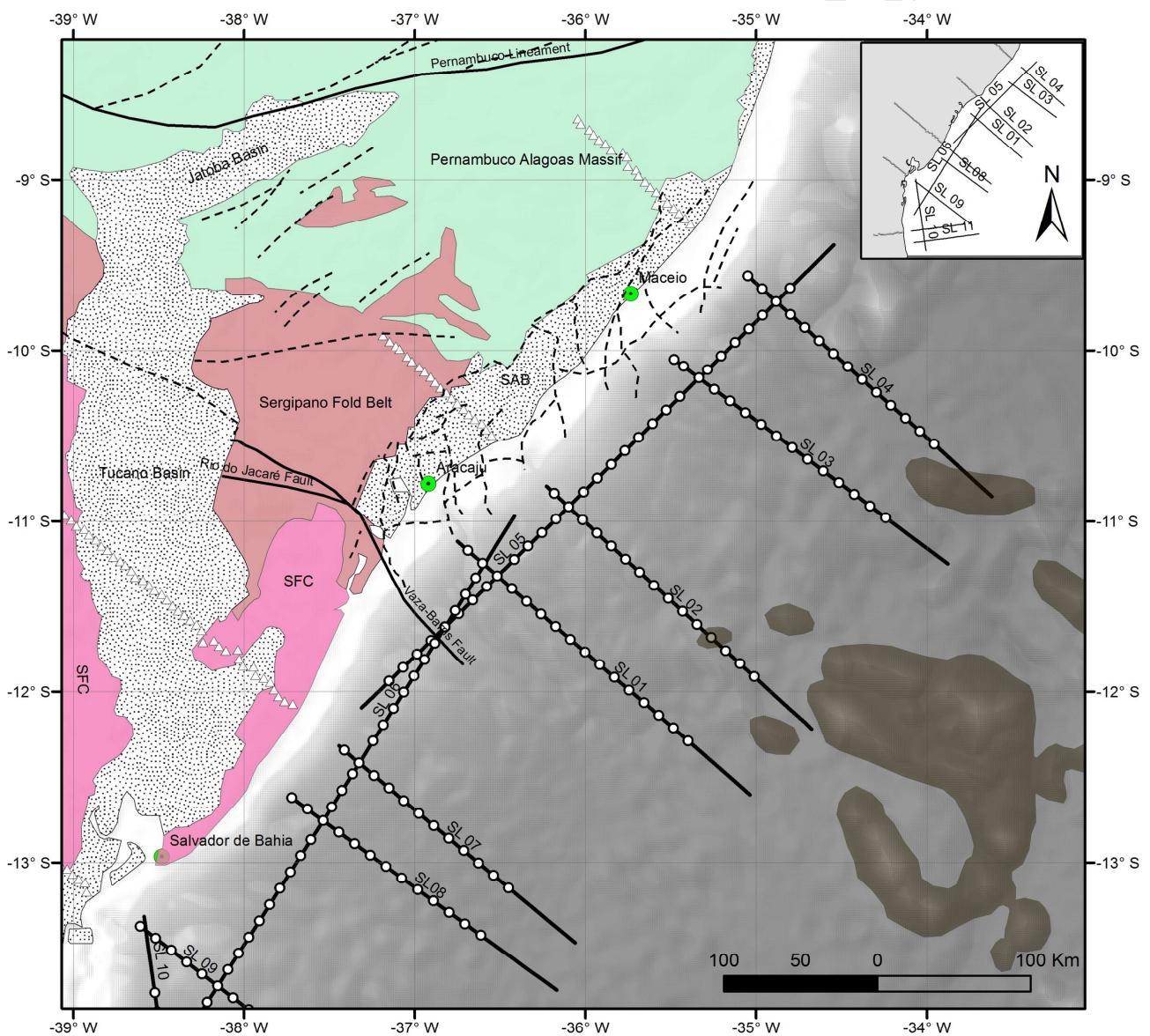
134 • Mohriak *et al.* (1998) observed some structures in the proximal deep-water basin that was  
135 interpreted as igneous bodies (Figure 3). One example is a plug interpreted as a post-rift volcanic  
136 intrusion close to the Continental Ocean Boundary (COB) (Figure 3). Bordering this plug, in the  
137 proximal side, there are packages of reflectors with a sigmoidal geometry, mostly dipping seawards,  
138 but also dipping landwards, that probably correspond to seaward-dipping-reflectors and landward  
139 dipping reflectors (SDRs and LDRs) (Figure 3), which were interpreted as formed by volcanic  
140 rocks extruded during early phases of spreading oceanic ridges (Mohriak *et al.*, 1998). These  
141 magmatic features are usually associated with extensional processes and oceanic crust inception,  
142 and therefore post-date the rift-phase lithospheric extension associated with the break-up of  
143 Gondwana in the Early Cretaceous. On the base of this observations, Mohriak *et al.* (1995)  
144 suggested that the central segment of the South Atlantic African margins could also be considered  
145 as a volcanic margin such as the Norwegian margin (e.g. Eldholm *et al.*, 1989), the Greenland  
146 margin (e. g. Korenaga *et al.*, 2000), the Aden margin (Tard *et al.*, 1991) or the Namibia margin  
147 (Bauer *et al.*, 2000; Austin and Uchupi, 1982). However, Moulin *et al.* (2005) have quoted the  
148 differences between the 4 km thick SDRs layer lying on top of a 30km-thick igneous crust and  
149 extending over a lateral distance of 150km on the Greenland margin (Korenaga *et al.*, 2000) and  
150 this less than 20km wide and less than 3km thick SDRs described by Mohriak *et al.* (1995). They  
151 argued that if their thickness is similar, their lateral extensions are quite different and the same  
152 genetic process can hardly be attributed to both structures.

153 • Assuming a simple geologic model based in thinning of the crust with mantle rising from 35  
154 km in the onshore region to about 25 km at the platform, and to about 20 km near the shelf edge, the  
155 gravity modelling for the Sergipe sub-basin and the Jacuipe Basin suggests a very rapid crustal  
156 thinning near the present-day shelf edge (Mohriak *et al.*, 1995, 1998). According to this modelling,  
157 the Moho topography gets more regular from slope to seawards with depths between 15 and 18 km  
158 across the COB (Figure 3).

159 • In addition to the rapid shallowing of the Moho and the presence of SDRs, the 2D gravity  
 160 modeling of Blaich *et al.* (2008) required the introduction of a lower crustal high-density body in  
 161 the proximal part of the gravimetric profile, in the necking zone, between 200 km and 300 km  
 162 distance (Figure 4). For these authors this high-density body would indicate a volcanic margin  
 163 character.

164 • The COB location was evaluated by this 2D gravity modelling (Blaich *et al.*, 2008) and  
 165 illustrates also a Moho discontinuity that shallows very rapidly eastward of the depocenter, rising  
 166 from 33 km to 18 km depth within a distance of about 70 km, not so different of the model  
 167 proposed by Mohriak *et al.* (1998).

168



### Legend

- △ Land Seismic Stations (LSS)
- Ocean Bottom Seismometer (OBS)
- Salsa profiles

### Structures

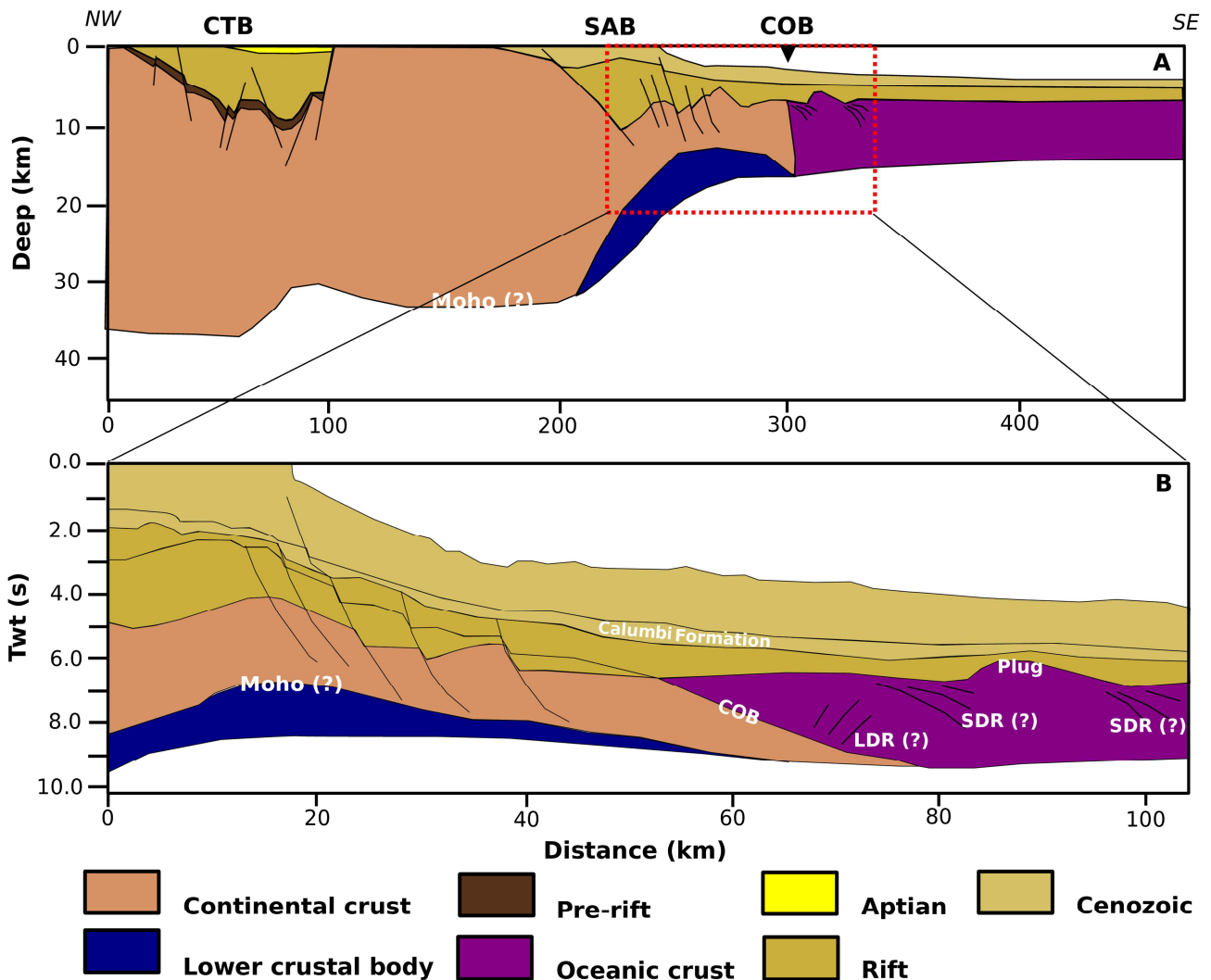
- Fractures and faults
- Principal lineaments and zones of transference

### Geology

- ▨ Cretaceous basins
- Proterozoic orogenic belts
- Palaeoproterozoic Borborema Province
- Palaeoproterozoic São Francisco Craton
- Bahia Seamounts

169

170 Figure 2. Geological Map of the Basin Sergipe-Alagoas and region around (modified from Lana, 1990,) with the  
 171 SALSA profiles, the principal faults and fractures, and the geological features associated with the São Francisco  
 172 Craton (SFC), the SFB and the Sergipe Alagoas Basin (SAB). Mercator projection.



173 Figure 3: a) Gravity modelled transect in SAB modified from Blaich et al. (2008), represented by the blue line in figure  
 174 1. The red dotted square in the gravity model represents the location of the seismic profile 239-RL-343, the area inside  
 175 the square was modelled based on seismic data and the rest on gravity data; b) Interpreted deep seismic profile 239-  
 176 RL-343 by Mohriak et al. (1995, 1998, 2000), represented by the red line in figure 1. CTB, Central Tucano Basin; SAB,  
 177 Sergipe Alagoas Basin; COB Continental-Oceanic Boundary; SDR, Seaward Dipping Reflectors; LDR, Landward  
 178 Dipping Reflectors.

179

## 180 Data Processing and Modeling

181 The ION-GXT profiles are high quality reflection seismic profiles. However, the time-to-depth  
 182 inversion made to transform the time data into depth data are not based on high-accuracy crustal P-  
 183 wave velocities. The SALSA refraction seismic profiles were located following some ION-GXT  
 184 profiles positions, allowing in the future an integration of more detailed crustal P-wave velocities

185 obtained by wide-angle refraction data. During the SALSA experiment, Multi-Channel Seismic  
186 (MCS) acquired jointly with refraction data was processed using the Geocluster (CGG Veritas)  
187 software. The processing sequence was composed of geometry, wave-equation multiple attenuation,  
188 shot-gather predictive deconvolution, time variant band-pass filter, random multiple attenuation,  
189 normal move-out, CMP stack and post-stack FK time migration. A last step of seismic data  
190 processing is the pre-stack depth migration of the MCS data using the results of wide-angle seismic  
191 data modeling, followed by residual move-out analysis. This procedure uses both near-vertical and  
192 wide-angle seismic data sets to produce a depth seismic section, which images both the sedimentary  
193 crust as well as the basement. Furthermore, it allows to verify the accuracy of the wide-angle  
194 velocity model in the sedimentary sequences.

195

## 196 **Results**

197 Despite the profiles SL01 and SL02 being parallel, 75 km apart, and in the same sedimentary basin,  
198 each multi-channel seismic image shows a very different sedimentary stratigraphy and basement  
199 geometry (Figure 4). While the southern SL01 MCS record-section shows some chaotic patterns,  
200 with heterogeneous layers, sometimes truncations, and a basement with a quite irregular  
201 topography, the SL02 MCS record-section, shows some plan-parallel layers (except the seafloor,  
202 that is quite irregular in the proximal part). Sometimes, there are some completely seismically  
203 transparent areas, which might be associated with erosional boundaries (Figure 4).

## 204 **SL01**

205 The SL01 line is a 210 km long and NW-SE oriented profile that spans from the continental slope to  
206 the distal basin. It is coincident with the ION-GXT 2275 profile and parallel to the associated SL02  
207 profile; both refraction profiles were planned to study the crustal architecture of the SAB (Figure 1).

208 At sea, a total of 16 OBS (instruments with four components: Hydrophone plus 3-Comp.  
209 Seismometer) were deployed, spaced every 13 km, at water depths of 1 560 m to 4 320 m. The 1376  
210 air-gun shots in SL01 were recorded by all instruments. The quality of the recorded signal is very  
211 good. This profile crosses two margin parallel profiles designed to image the segmentation (Evain  
212 *et al.*, in prep.): the SL06 profile at the SL01OBS02 and the SL05 profile at the SL01OBS03 in the  
213 proximal part.

214 In the OBS data, several near-offset reflected and associated refracted arrivals are visible,  
215 decreasing in number as we move towards the distal basin.

216 From SL01OBS01 onward, the full subsurface sedimentary, crustal, and mantellic sequence is  
217 imaged from shots at the vertical of each OBS to offsets reaching 110 km. In addition to clear Pg1,  
218 Pg2, Pg3, Pu, Pn (mostly) first arrivals (represented with blue, violet and magenta shades), Ps1 to  
219 Ps6 sedimentary refracted arrivals, traveling with apparent velocity increasing from less than 2 km/s  
220 (close to the water-cone) up to 3 km/s, are observed as secondary arrivals (represented with red,  
221 orange, yellow, and light-green shades). The shallowest layer, is very slow (1.85 km/s) and not very  
222 well marked on the seismic profile, but is necessary to fit correctly the secondary later arrivals.  
223 From the second to fifth layer, the velocity increases from 2.00 km/s to 3.10 km/s. From  
224 SL01OBS01 to SL01OBS03, these layers do not show evidence of clear refracted arrivals and were  
225 positioned according to the reflected arrivals. The Ps6 refraction shows top and bottom velocities  
226 from 3.35 km/s to 3.45 km/s. Furthermore, at near-critical incidence, high-amplitude reflections are  
227 observed, particularly from the tops of the lower crust Pg3P, Unknown unit PuP, and Moho PmP on  
228 the seaward-side of OBSs. The Pg1 phase presents the shortest offset span (from ~7.5 to 20 km  
229 offset, as we can see in the SL01OBS03 (Figure 5); and the largest curvature indicative of larger  
230 velocity gradient. The Pg2 extends from 20 to ~50 km offset and Pg3 from 50 to ~80 km offset and  
231 present the lowest apparent velocity gradient.

232 In the distal oceanic part, from 90 to 220 km model distance, from SL01OBS08 (Figure 6) to  
233 SL01OBS15 (Figure 7), the data shows only four sedimentary layers and the related phases, Ps1 to  
234 Ps4 remain weak, and almost indistinguishable refracted arrival phases that are recorded as a fan of  
235 second arrival phases with slightly increasing velocities and relatively low velocity-gradients that  
236 emerges from the water cone. These phases were also modelled according to the reflected arrivals..  
237 In the presumed oceanic basin, the Pg1, Pg2 and Pg3 refracted phases form a relatively continuous  
238 event in both amplitude and apparent velocity, without sharp inflections indicative of major velocity  
239 changes between layers. The PuP phase spans from 0 to 80 km model distance with apparent  
240 velocity close to Pg3 in the necking zone. Pn is observed emerging at ~70 km offset with an  
241 apparent velocity increasing from 7.90 to more than 8.10 km/s and large amplitude variations both  
242 along offset and OBSs.

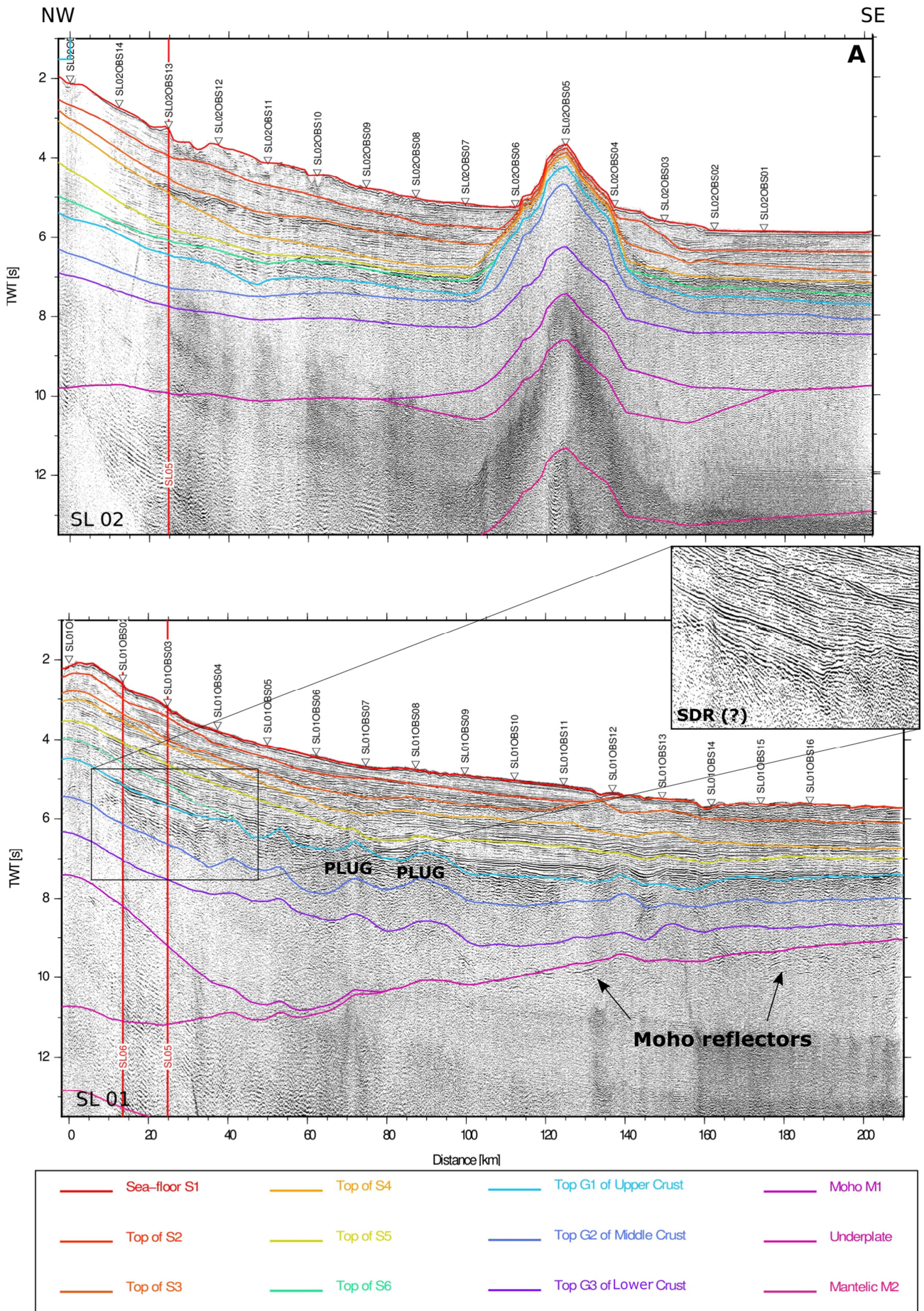
243

244

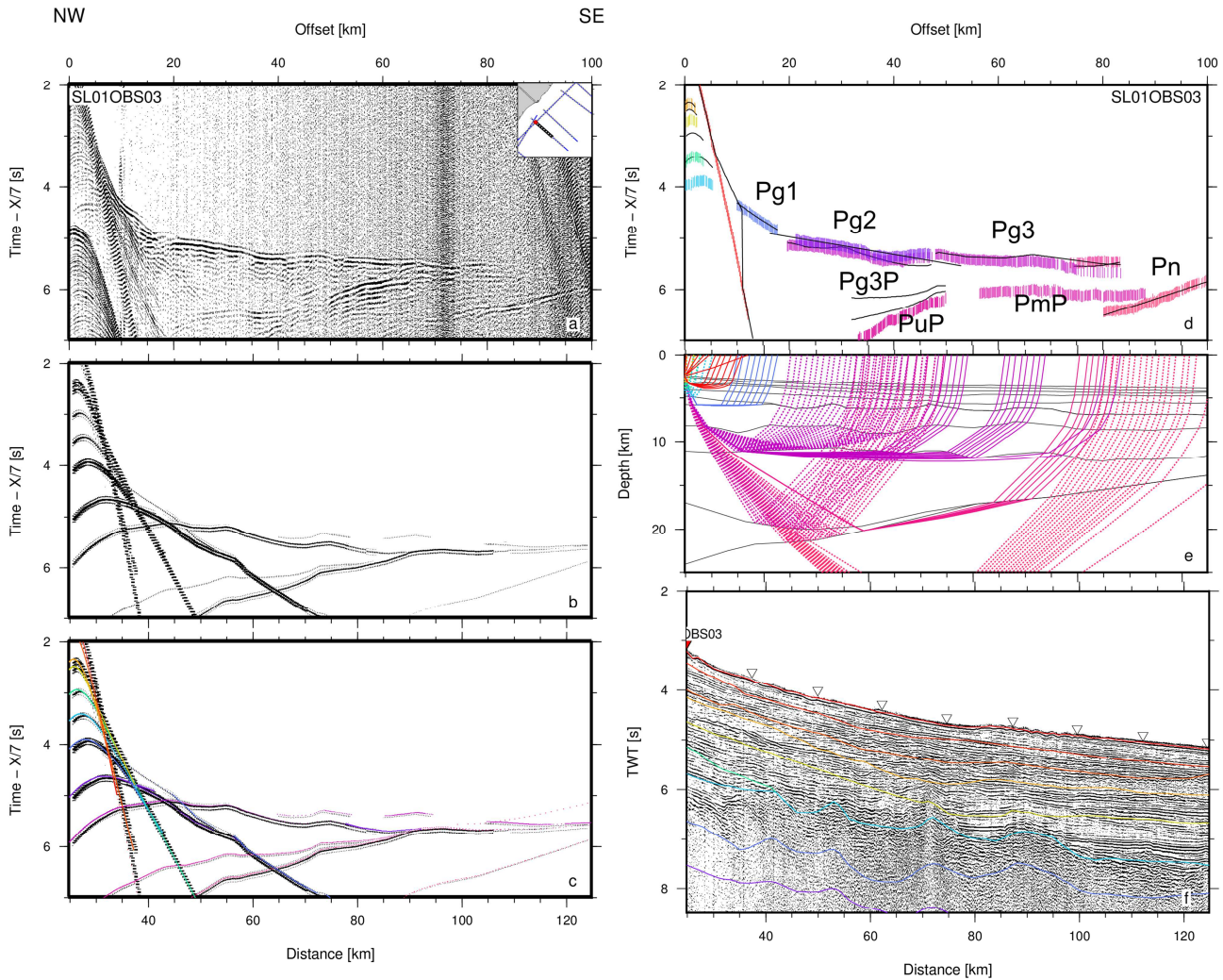
245

246

247



249 *Figure 4: Two-way travel-time record section of MCS data along SL02 (A) and SL01 (B) profiles overlain by time*  
 250 *converted interfaces of wide-angle model. The intersections with the SALSA dataset are indicated by red line.*  
 251 *OBS locations are indicated by white triangle. Vertical exaggeration at seafloor is 1 :12.5*



252 *Figure 5: SL01OBS03 on profile SL01 on the SAB. a) Seismic record; b) Synthetics; c) Color coded synthetic; d) Color*  
 253 *coded observed travel-times overlain by predicted times in black; e) Seismic rays; f) MCS time migrated section and*  
 254 *color-coded model interfaces. On a, b, c, and d, travel-time is reduced by a velocity of 7 km/s.*

### 255 **Velocity model**

256 From SL01 wide-angle data, we digitized 25741 events and interpreted their respective phases.  
 257 Travel-time uncertainty was estimated on the SL01OBS records and fixed at 0.030 s for the water,  
 258 0.050 s for the sedimentary arrivals increasing to 0.100 s for the crustal and mantellic arrivals. The  
 259 model explains the travel-time and phase of 21204 events or 82% of total picks, with a global RMS  
 260 travel-time residual of 0.119 s. Given our events individual uncertainty, the model results in a  
 261 normalized chi-squared of 1.406. Generally, the SL01 model correctly explained the SL01OBS with  
 262 chi-squared and rms acceptable values (Table 1).

263 The final velocity model of profile SL01 images all the sedimentary and basement layers to a depth  
 264 of around 25 km (Figure 8B).

265 The model has a sedimentary cover with 6 sedimentary layers in the continental part and 4 layers in  
 266 the presumed oceanic basin, that reach a thickness of 5 km for all along the profile. S1 has no lateral  
 267 velocity gradient with top and bottom seismic velocities of 1.75 km/s to 1.80 km/s. S2 has a lateral  
 268 gradient in the velocities that goes from 2.00 km/s in the western part of the profile and gradually  
 269 decreases up to 1.80 km/s. The two first sedimentary layers pinch out at 130 km in the distal basin.

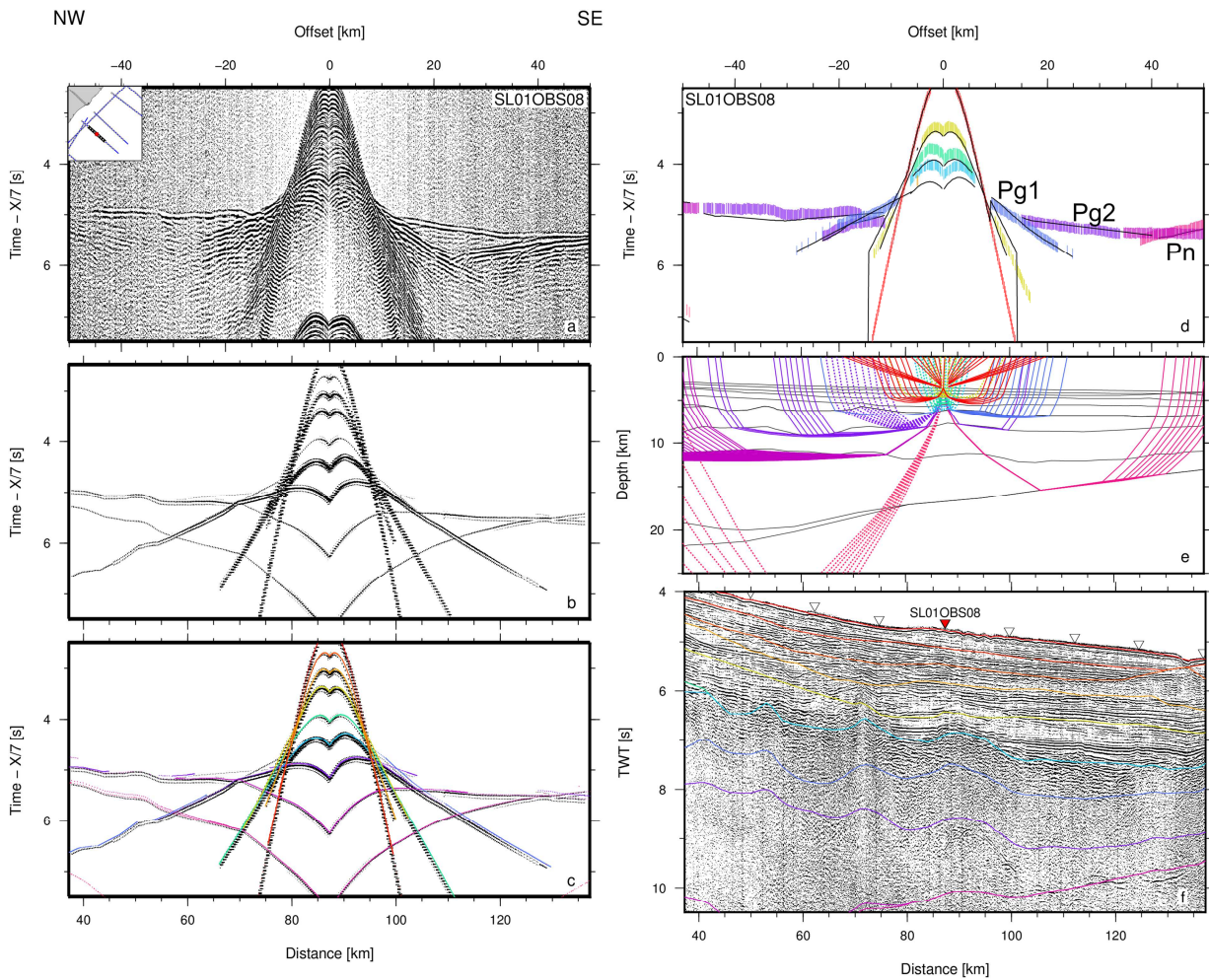
phase	npts	Trms (s)	chi-squared	Uncertainty (ms)	
water	2112	0.028	0.080	30	270
Ps1P	264	0.091	0.827	50	271
Ps2P	10	0.076	0.641	50	272
Ps3P	527	0.087	0.751	50	273
Ps4P	672	0.186	3.463	50	274
Ps5P	243	0.097	0.943	50	275
Ps6P	682	0.252	6.379	50	276
Pg13	810	0.106	1.122	100	277
Pg1P3	1582	0.104	1.081	100	278
Pg23	1507	0.100	1.008	100	279
Pg33	2173	0.100	1.004	100	280
Pg3P3	4916	0.127	1.605	100	281
Pn3	3048	0.113	1.274	100	
PmP3	535	0.204	4.163	100	
Pu3	419	0.222	4.924	100	
Pup4	1483	0.242	5.859	100	

282 *Table 1: Reflected or refracted phase name, number of explained events, residual mean-square, and normalized chi-*  
 283 *squared value for the SL01 model.*

284 S3 has top and bottom velocities from 2.40 km/s to 2.50 km/s. S4 has regular top and bottom  
 285 velocities from 2.85 km/s to 3.00 km/s. S5 has also regular top and bottom velocities from 3.10  
 286 km/s to 3.15 km/s on the distal basin and a constant velocity of 2.95 km/s on the continental slope.  
 287 S6 appears only in the continental slope zone, over a basement depression, and pinches out at 40 km  
 288 and has top and bottom velocities from 3.35 km/s to 3.45 km/s.

289 The lithospheric structure has five layers: upper crust, middle crust, lower crust, anomalous velocity  
 290 zone and lithospheric mantle. The upper crust has a thickness of 2.5 km on the continental slope and  
 291 decreases to 1.0 km and 1.5 km on the distal basin with a very irregular topography, full of basins  
 292 and mounts, with velocities at the top and bottom of 5.00 km/s and 5.10 km/s, a little decrease to  
 293 4.85 km/s at 110 km and increases to 5.10 km/s and 5.20 km/s at the distal basin. The middle crust  
 294 has regular thickness of 2.5 km for all along the profile, with velocities at the top and bottom from  
 295 6.50 km/s to 6.60 km/s. The lower crust starts with a thickness of 5 km in the very northwestern

296 part of the profile, and thickens to 10 km between 20 and 70 km and thins to 3.0 km towards the  
 297 ocean, with velocities at the top and bottom from 7.00 km/s to 7.20 km/s.



298 *Figure 6: SL01OBS08 on profile SL01 on the SAB. a) Seismic record; b) Synthetics; c) Color coded synthetic; d) Color*  
 299 *coded observed travel-times overlain by predicted times in black; e) Seismic rays; f) MCS time migrated section and*  
 300 *color-coded model interfaces. On a, b, c, and d, travel-time is reduced by a velocity of 7 km/s.*

301

302

303

304

305

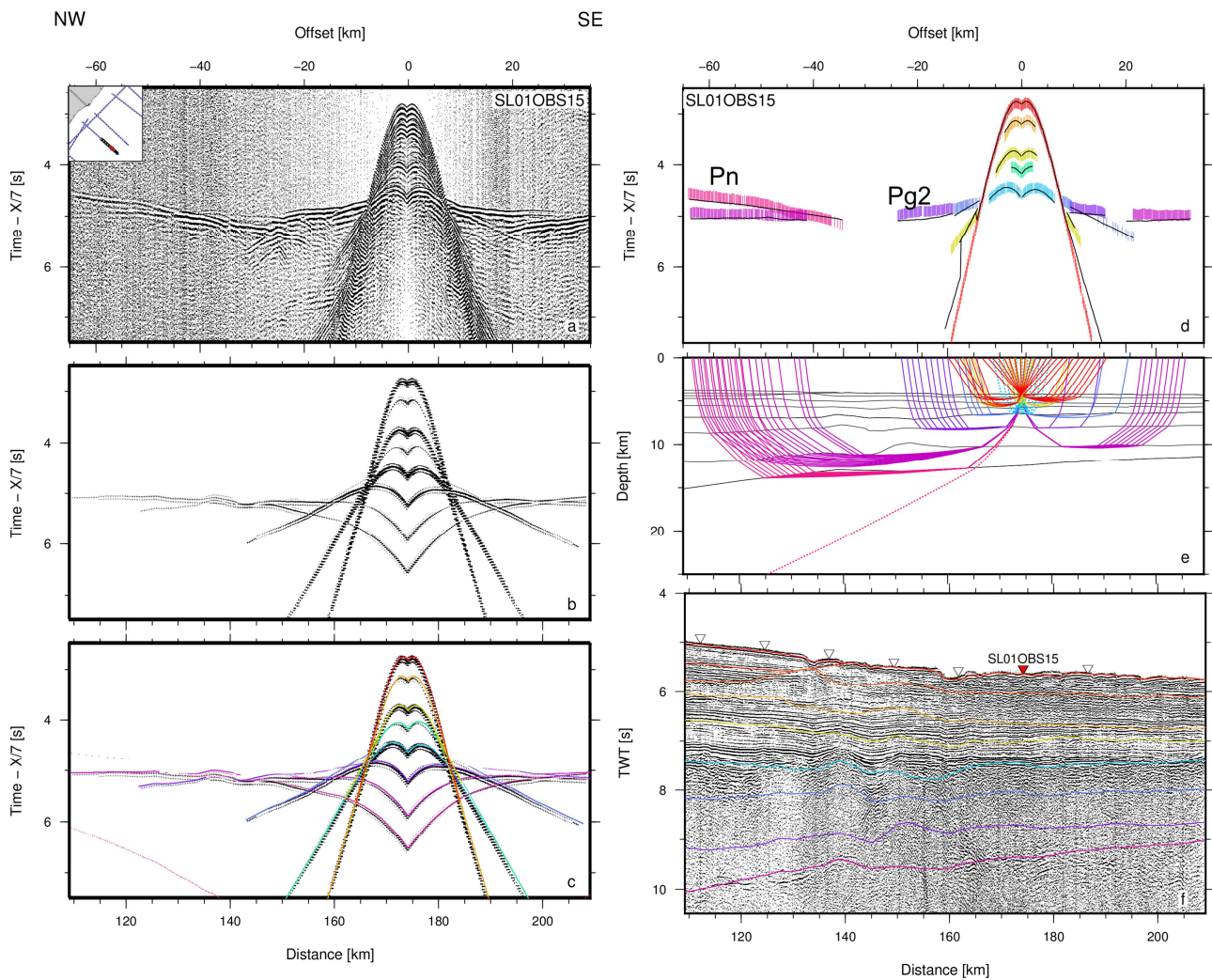
306

307

308

309

310



312

313 *Figure 7: SL01OBS15 on profile SL01 on the SAB. a) Seismic record; b) Synthetics; c) Color coded synthetics; d)*  
 314 *Color-coded observed synthetic; d) Color coded observed travel-times overlain by predicted times in black; e) Seismic*  
 315 *rays; f) MCS time migrated section and color-coded model interfaces. On a, b, c, and d, travel-time is reduced by a*  
 316 *velocity of 7 km/s.*

317 The anomalous velocity zone, located at the necking zone, is badly constrained, showing its  
 318 possible reflected arrival only in the two most proximal OBSs. These reflected arrivals can also be  
 319 the result of an internal reflector, representing some intra-crustal body. With this information and  
 320 the ION-GXT data (Figure 8B), this zone was modeled with 10 km thickness, that thins abruptly  
 321 until pinching out against the lower crust at 80 km. This zone presents velocities between the top  
 322 and the bottom from 7.20 km/s to 7.25 km/s. The top of the lithospheric mantle below the Moho has  
 323 a velocity of 7.90 km/s. Note that an additional lithospheric layer located at 10 to 15 km below the  
 324 Moho, with 8.10 km/s, is necessary to provide a gradient capable of explaining the Pn arrivals. It is

325 well constrained in the proximal part of the two profiles, but only in the distal part of SL02 profile  
326 (Figure 8A).

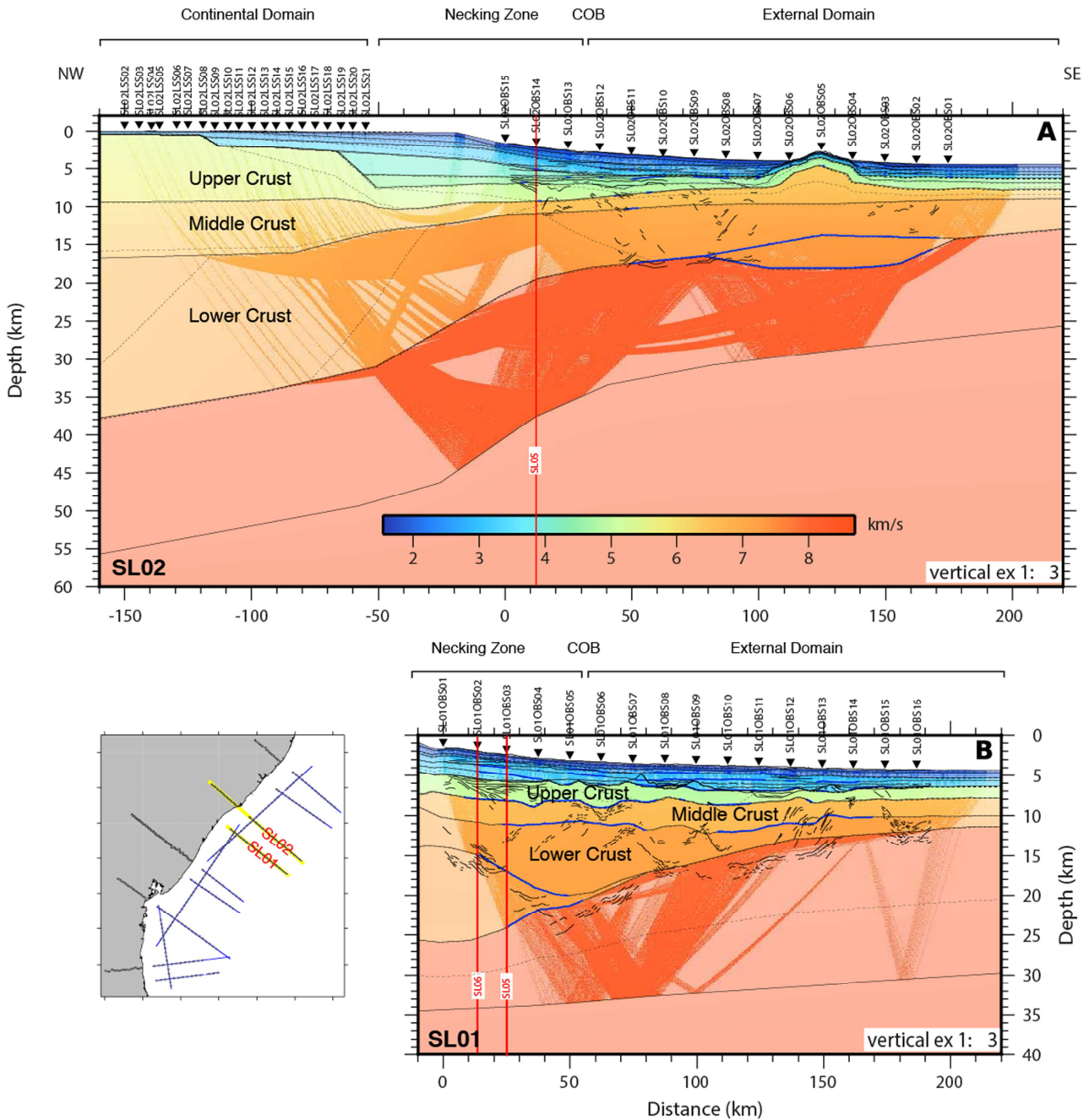
327

## 328 **SL02**

329 The SL02 line is a 220 km long and NW-SE oriented profile, parallel to SL01, that spans offshore  
330 from the continental platform to the distal basin. The SL02 was extended inland along a distance of  
331 150 km from the most proximal OBS, for a total profile length of 370 km. It is coincident with the  
332 ION-GXT 2300 profile (Figure 8A).

333 At sea, a total of 15 OBS (instruments with four components: Hydrophone plus 3-Comp.  
334 Seismometer) were deployed, spaced every 13 km, at water depths of 1.557 to 4.368 m (Figure 1C).  
335 The 1271 air-gun shots in SL02 were recorded by all instruments. The quality of the recorded signal  
336 is very good. Inland, the profile was extended 150 km towards the North-West with the deployment  
337 of 21 Land Seismic Stations (LSS, spaced every 5 km). The profile has 100 km of extension  
338 because, unfortunately, there is a gap of about 50 km between the last LSS and the first OBS, on the  
339 inner shelf. This profile crosses the SL05 profile at the position of the SL02OBS02 and  
340 SL05OBS14, in proximal position.

341 The geometry of the sedimentary and crustal layers onland beneath the seismic land stations can  
342 further be constrained from geological and geophysical studies conducted in the study area (Chang  
343 *et al.*, 1992; Soares *et al.*, 2010; Tavares *et al.*, 2012; de Lima *et al.*, 2015). Surface geology  
344 indicates the Sergipano Fold Belt from SL02LSS11 to SL02LSS01, and an outcrop of Quaternary  
345 deposits from SL02LSS21 to SL02LSS10, as shown at the SL02LSS15 (Figure 9).

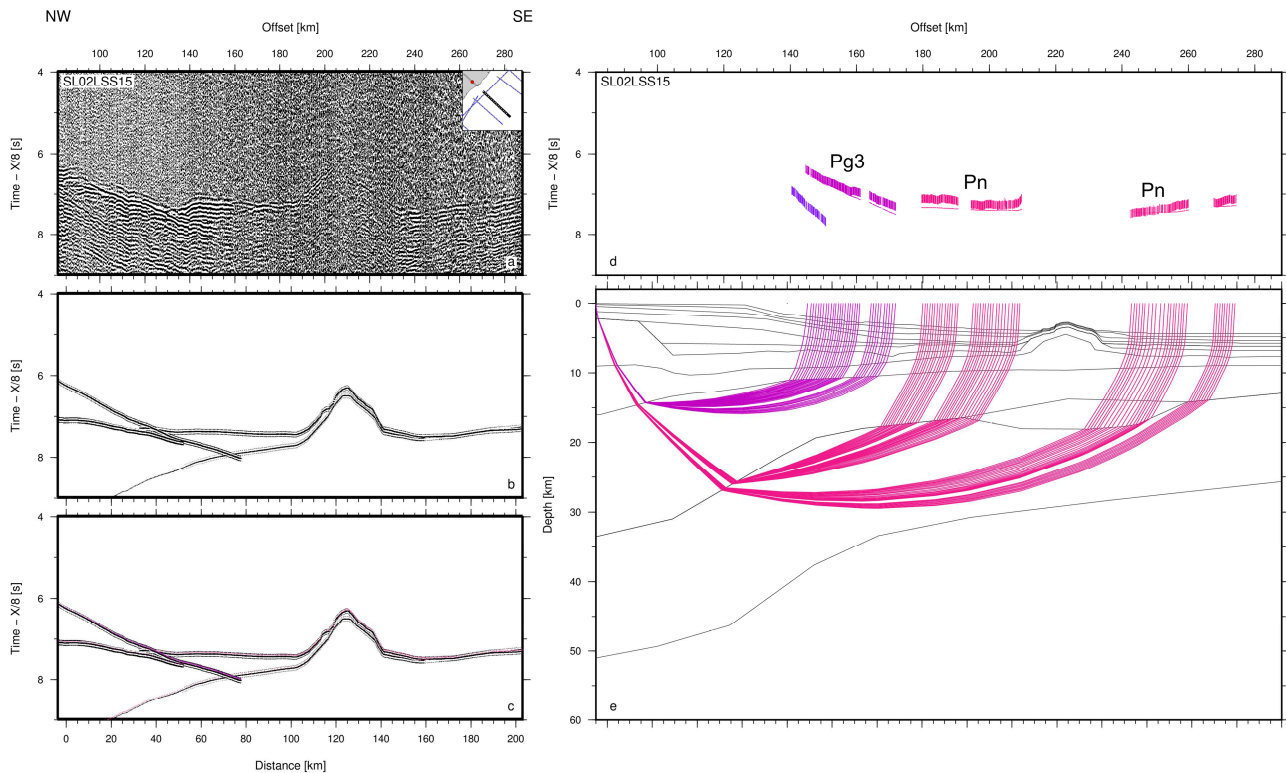


347 Figure 8: Final P-wave interval velocity models along SL02 (A) and SL01 (B) profiles overlaid by the respective line-  
 348 drawing of the ION-GXT lines. Black lines mark model layer boundaries. Colored area is constrained by seismic rays.  
 349 Inverted black triangle mark OBS and LSS positions. Thick blue lines mark the interfaces where reflections are  
 350 observed on the wide-angle records. Black dotted lines correspond to isocontours. Vertical red lines indicate crossing  
 351 profiles. Vertical exaggeration is 1:3.

352

353 Refracted events in the continental crust middle-crust Pg2 in light-blue, lower-crust Pg3 in blue and  
 354 Pn in violet are relatively strong and allow to constrain the crustal structure from -160 to 0 km  
 355 model-distance (Figure 9). Pn arrivals refracted from as deep as 30 km beneath the un-thinned

356 continental margin traveling at 8 km/s apparent velocity. PmP arrivals from 150-160 km offset  
 357 reflect from the hinge-line where the continental crust begins to thin.



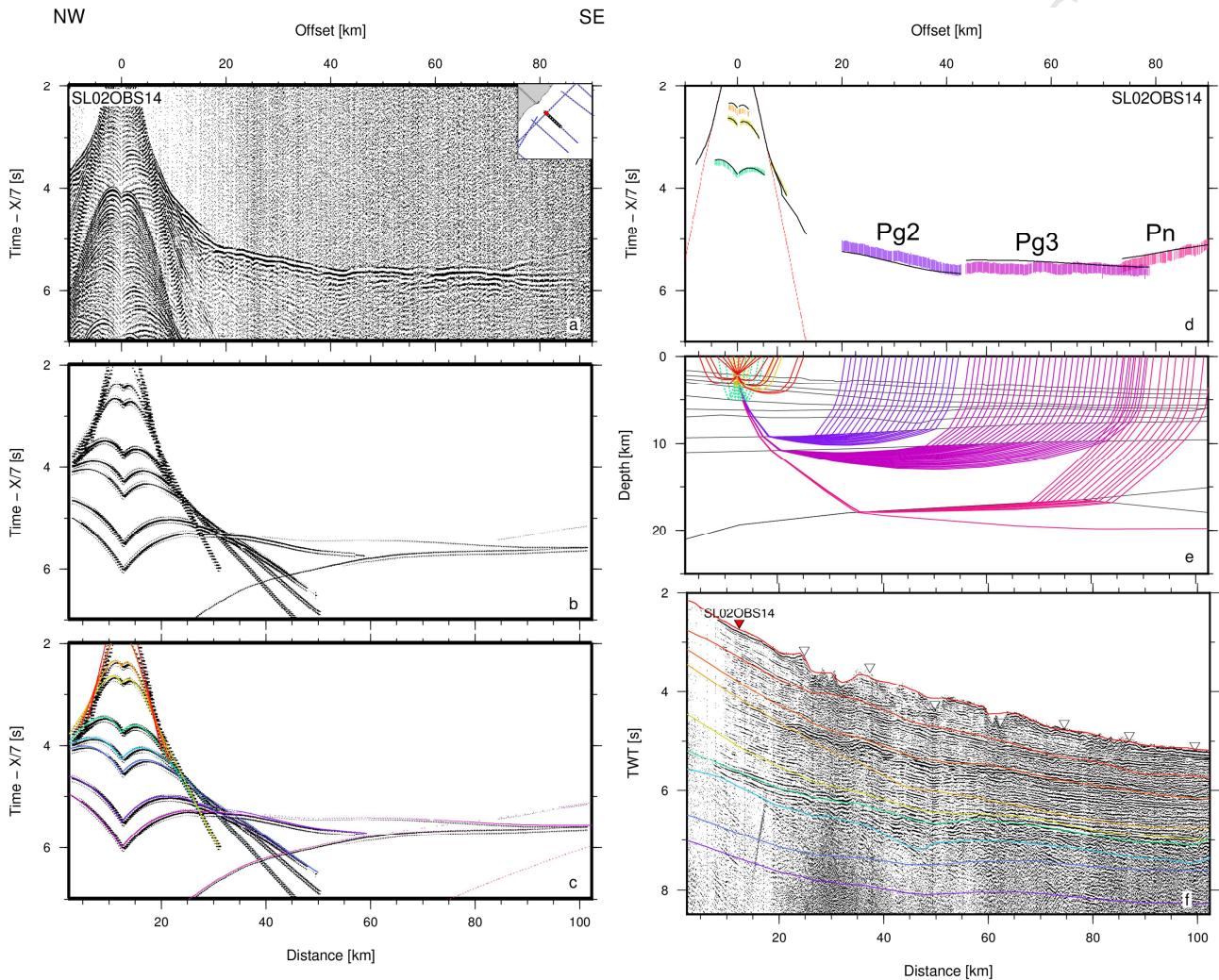
358 *Figure 9: SL02LSS15 on profile SL02 on the SFB/SAB contact. a) Seismic record; b) Synthetics; c) Color coded*  
 359 *synthetic; d) Color coded observed travel-times overlain by predicted times in black; e) Seismic rays. On a, b, c, and d,*  
 360 *travel-time is reduced by a velocity of 8 km/s.*

361

362 From SL02OBS15 onward, the full subsurface sedimentary, crustal and mantellic sequence is  
 363 imaged from shots at the vertical of each OBS to offsets reaching 110 km. The SL02OBS14 (Figure  
 364 10) shows the example of this part. In addition to clear Pg1, Pg2, Pg3, Pu, Pn (mostly) first arrivals  
 365 (represented with blue, violet and magenta shades), Ps1 to Ps6 sedimentary refracted arrivals,  
 366 traveling with apparent velocity increasing from less than 2 km/s (close to the water-cone) up to 4  
 367 km/s, are observed as secondary arrivals (represented with red, orange, yellow, and light-green  
 368 shades). At ~60 km distance, the Ps5 disappears, and the profile continues seawards with only 5  
 369 sedimentary layers. Furthermore, at near-critical incidence, high-amplitude reflections are observed,  
 370 particularly from the tops of the lower crust Pg3P, unknown unit PuP, and Moho PmP on the  
 371 seaward-side of OBSs. The Pg1 phase presents the shortest offset range (from ~7.5 to 20 km offset),  
 372 and the largest curvature indicative of large velocity gradient. The Pg2 extends from 20 to ~40 km  
 373 offset and Pg3 from 45 to ~80 km offset and the lowest apparent velocity gradient.

374 In the distal part, from 90 to 140 km model distance, as shown in SL02OBS07 (Figure 11), the Ps1  
 375 to Ps4 remain weak and almost undistinguishable refracted arrival phases that are recorded as a fan  
 376 of second arrivals with slightly increasing velocities and relatively low velocity-gradients that

377 emerges from the water cone. The Ps5 refraction shows considerably higher amplitude and apparent  
 378 velocity: the exact nature of the S6 layer represented by this phase must be further examined from  
 379 the pre-stack depth migration of the MCS data, for instance. In the distal oceanic part, the Pg1, Pg2  
 380 and Pg3 refracted phases form a relatively continuous event in both amplitude and apparent  
 381 velocity, without sharp inflections indicative of major velocity changes between layers. The Pu  
 382 phase spans from 90 to 140 km offset and has an apparent velocity close to Pg3. Pn is observed



383 emerging at  $\sim 75$  km with an apparent velocity increasing from 7.9 to more than 8.15 km/s and large  
 384 amplitude variations both along offset and OBSs.

385 *Figure 10: SL02OBS14 on profile SL02 on the SAB. a) Seismic record; b) Synthetics; c) Color coded synthetic; d)*  
 386 *Color coded observed travel-times overlain by predicted times in black; e) Seismic rays; f) MCS time migrated section*  
 387 *and color-coded model interfaces. On a, b, c, and d, travel-time is reduced by a velocity of 7 km/s.*

388

### 389 **Velocity Model**

390 From SL02 wide-angle data, we digitized 24009 events and interpreted their respective phases.  
 391 Travel-time uncertainty was estimated on the SL02OBS and SL2LSS records and fixed at 0.030 s  
 392 for the water, 0.050 s for the sedimentary arrivals increasing to 0.100 s for the crustal and mantellic

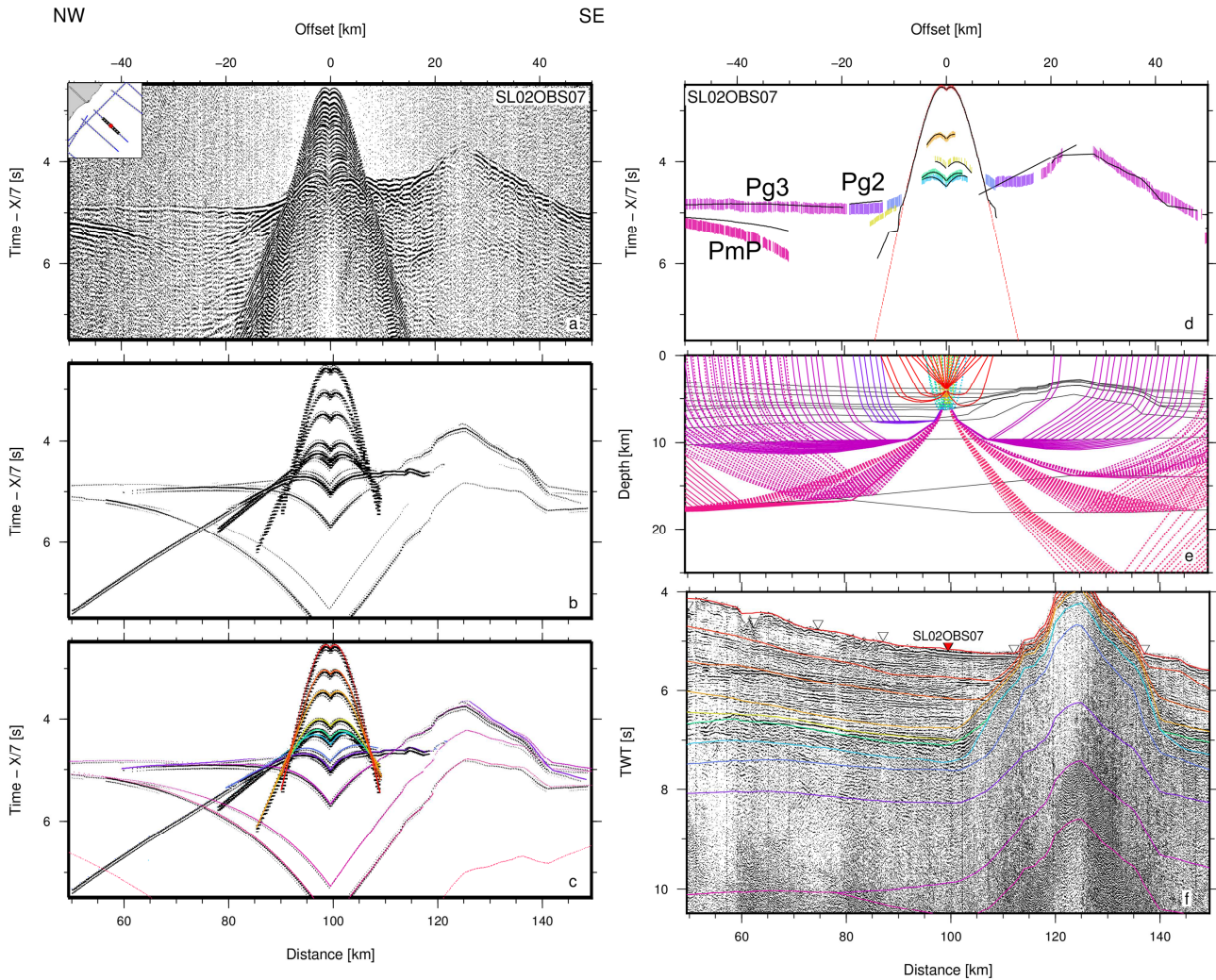
393 arrivals. The model explains the travel-time and phase of 21166 events or 88% of total picks, with a  
 394 global RMS travel-time residual of 0.138 s. Given our events individual uncertainty, the model  
 395 results in a normalized chi-squared of 1.892. Generally, the SL02 model correctly explained the  
 396 SL02OBS and SL02LSS with chi-squared and rms values acceptable (Table 2).

phase	npts	Trms	chi-squared	Uncertainty (ms)
water	2708	0.029	0.084	30
Ps1P	21	0.013	0.017	50
Ps2P	436	0.070	0.496	50
Ps3P	305	0.085	0.727	50
Ps4P	298	0.067	0.444	50
Ps5P	122	0.154	2.394	50
Ps6P	277	0.102	1.042	50
Pg1	43	0.113	1.308	100
Pg1P	32	0.186	3.570	100
Pg2	347	0.167	2.793	100
Pg2P	30	0.052	0.282	100
Pg3	1893	0.131	1.706	100
Pg3P	1980	0.121	1.470	100
Pn	7194	0.121	1.462	100
PmP	1083	0.145	2.101	100
Pu	38	0.052	0.274	100
PuP	1078	0.243	5.906	100

397 *Table 2: Reflected or refracted phase name, number of explained events, residual mean-square, and normalized chi-*  
 398 *squared value.*

399

400 The final velocity model of profile SL02 images the depth geometry of all sedimentary, crustal and  
 401 mantellic layers to a depth of around 34 km (Figure 8A). According to the interpretation of the  
 402 wide-angle data described above the velocity structure of SL02 model was modeled using four to  
 403 six layers of sediments. These sedimentary layers are characterized by relatively homogeneous P-  
 404 wave velocities all along the SL02 model with no strong lateral variation. This sedimentary deposit  
 405 in the SAB starts at -120 km model distance and reaches a maximum of 7 km of thickness between  
 406 -50 and -20 km model distance until 2.5 km at the SE in the distal basin (Figure 8A).



407

408 *Figure 11: SL02OBS07 on profile SL02 on the SAB. a) Seismic record; b) Synthetic; c) Color coded synthetic; d) Color*  
 409 *coded observed travel-times overlain by predicted times in black; e) Seismic rays; f) MCS time migrated section and*  
 410 *color-coded model interfaces. On a, b, c, and d, travel-time is reduced by a velocity of 7 km/s.*

411

412 The P-wave velocities of the sedimentary sequence show an increasing trend: the top velocity at the  
 413 seafloor is 1.65 km/s (S1) and the maximum velocity 4.7 km/s is reached at the base of the  
 414 sedimentary sequence (S6).

415 S1 has top and bottom P wave seismic propagation velocities of 1.65 km/s to 1.85 km/s. S2 has a  
 416 negligible vertical gradient and propagation velocity of 2.2 km/s on the western end of the profile  
 417 that gradually decreases up to 2.10 km/s. S3 has top and bottom velocities from 2.60 km/s to 2.70  
 418 km/s with a small gradient decrease towards the continental slope. S4 has top and bottom velocities  
 419 from 3.00 km/s to 3.25 km/s. S5 has top and bottom velocities from 4.10 km/s to 4.20 km/s. S6 has  
 420 constant top and bottom velocities from 4.60 km/s to 4.70 km/s.

421 Beneath this sedimentary record, the top of the basement corresponds to a rough interface and the  
422 modeled basement structure comprises four crustal layers: upper crust, middle crust, lower crust and  
423 an anomalous body under the volcano. The upper crust has a thickness between 1.0 km and 2.0 km  
424 on the presumed oceanic basin and increases to 3.0 km at the continental slope, with velocities at  
425 the top and bottom from 4.75 km/s to 5.1 km/s.

426 The middle crust has a regular thickness of 3.0 km for all the profile, except under the volcano,  
427 where it reaches almost 5.0 km with velocities at the top and bottom from 6.4 km/s to 6.5 km/s on  
428 the continental slope and from 6.2 km/s to 6.3 km/s on the distal basin. The lower crust is 8.0 km  
429 thick at the northwestern end of the model and completely thins out to 4.0 km thick towards the  
430 ocean, with velocities at the top and bottom from 6.90 to 7.10 km/s along all the profile, except in  
431 the necking zone, between 0 and 50 km model distance, where there is a slight increase of the  
432 velocities in the middle and the lower crusts: the middle crust passes from 6.10-6.30 km/s to 6.30-  
433 6.50 km/s and the lower crust, from 6.90-7.10 km/s to 7.30-7.50 km/s (Figure 8B). Note that there  
434 is also a thick anomalous body, not located below the Necking Zone as along SL01 profile, but  
435 below the Moho in the volcanic edifice area. It has a thickness of 8 km and velocities between 7.3-  
436 7.4 km/s.

## 437 Evaluation of the models

### 438 Gravity modelling

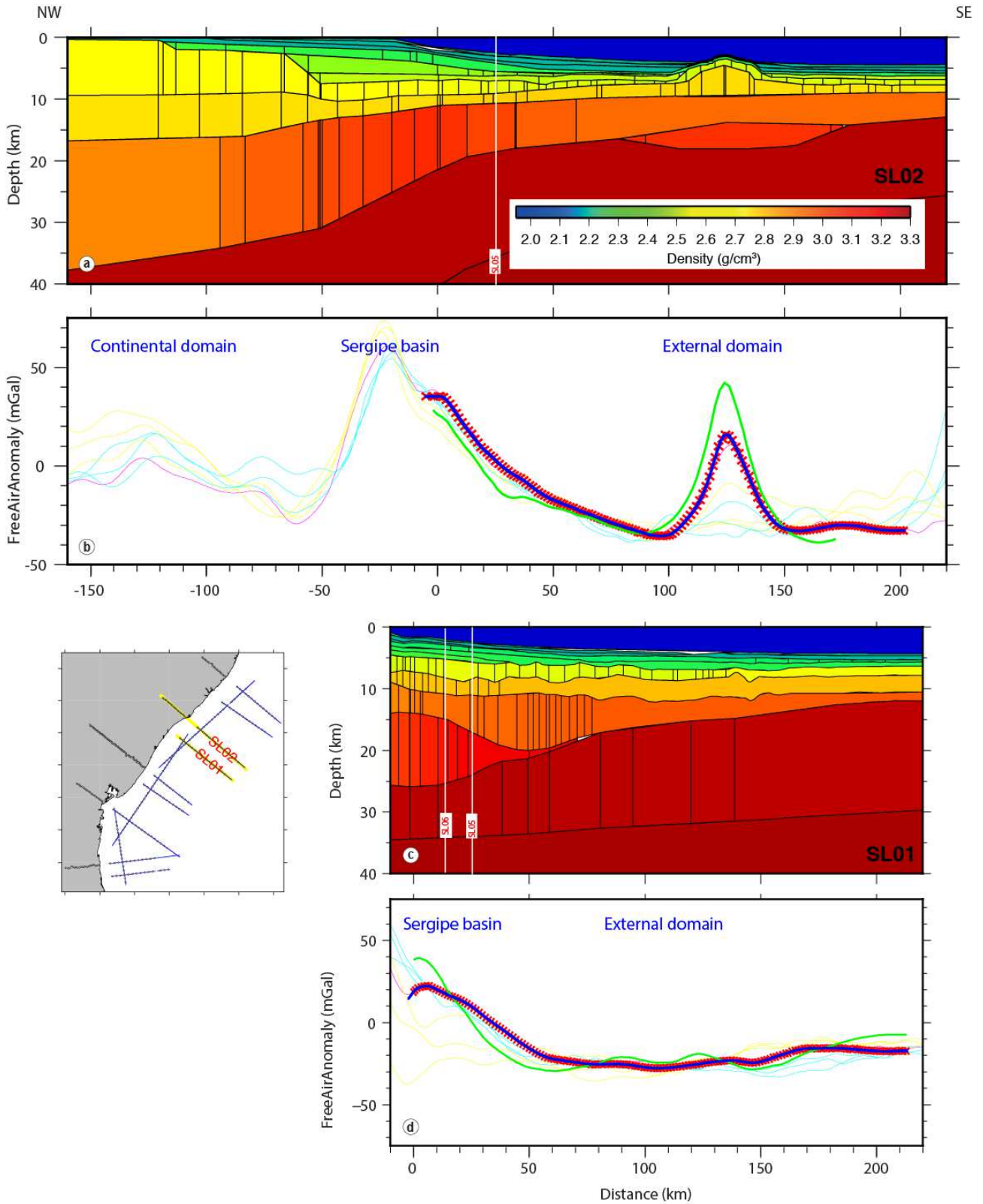
439 A 2-D model consisting of homogeneous density blocks was constructed from the seismic velocity  
440 model: the P-wave velocity is converted to densities according to Ludwig *et al.* (1970) except  
441 onshore in the continental crust where conversion follows Christensen and Mooney (1995). The  
442 resulting density ranges from 2200 to 2500 kg/m<sup>3</sup> in the basin, 2600 to 2750 kg/m<sup>3</sup> in the crust and  
443 3000 to 3170 kg/m<sup>3</sup> in the under-crustal unit. The mantle density is set at 3420 kg/m<sup>3</sup>. The model is  
444 extended down to 80 km where isostatic compensation may be reached, and the modeled free-air  
445 anomaly is compared to measured gravity anomaly along the SL01 and SL02 profiles (Figure 12).

446 The SL01 model fits relatively well (within less than 10 mGal) the gravity data acquired offshore  
447 during the SALSA survey, except for the continental slope (where the model is less constrained)  
448 where there's a misfit of 17 mGal. Free air gravity from satellite data (Sandwell *et al.*, 2014)  
449 extracted along the profile and 10, 20, and 30 km cross-line presents broad (>50 km wavelength)  
450 along profile and lateral scatter amplitude variations of +/- 10 mGal (Figure 12c and d).

451 The SL02 model fits relatively well (within less than 25 mGal) the gravity data acquired offshore  
452 during the SALSA survey, except for the seamount where there's a misfit of 65 mGal, probably due  
453 to the 3D effects. The calculated gravity anomaly falls well within the values observed on parallel

454 profiles extracted north and south of the profile (Figure 12a and b), derived from satellite gravity  
 455 measurements (Sandwell *et al.*, 2014). Due to the high altitude of the satellite, lower wave-length  
 456 are not well recorded.

457



458

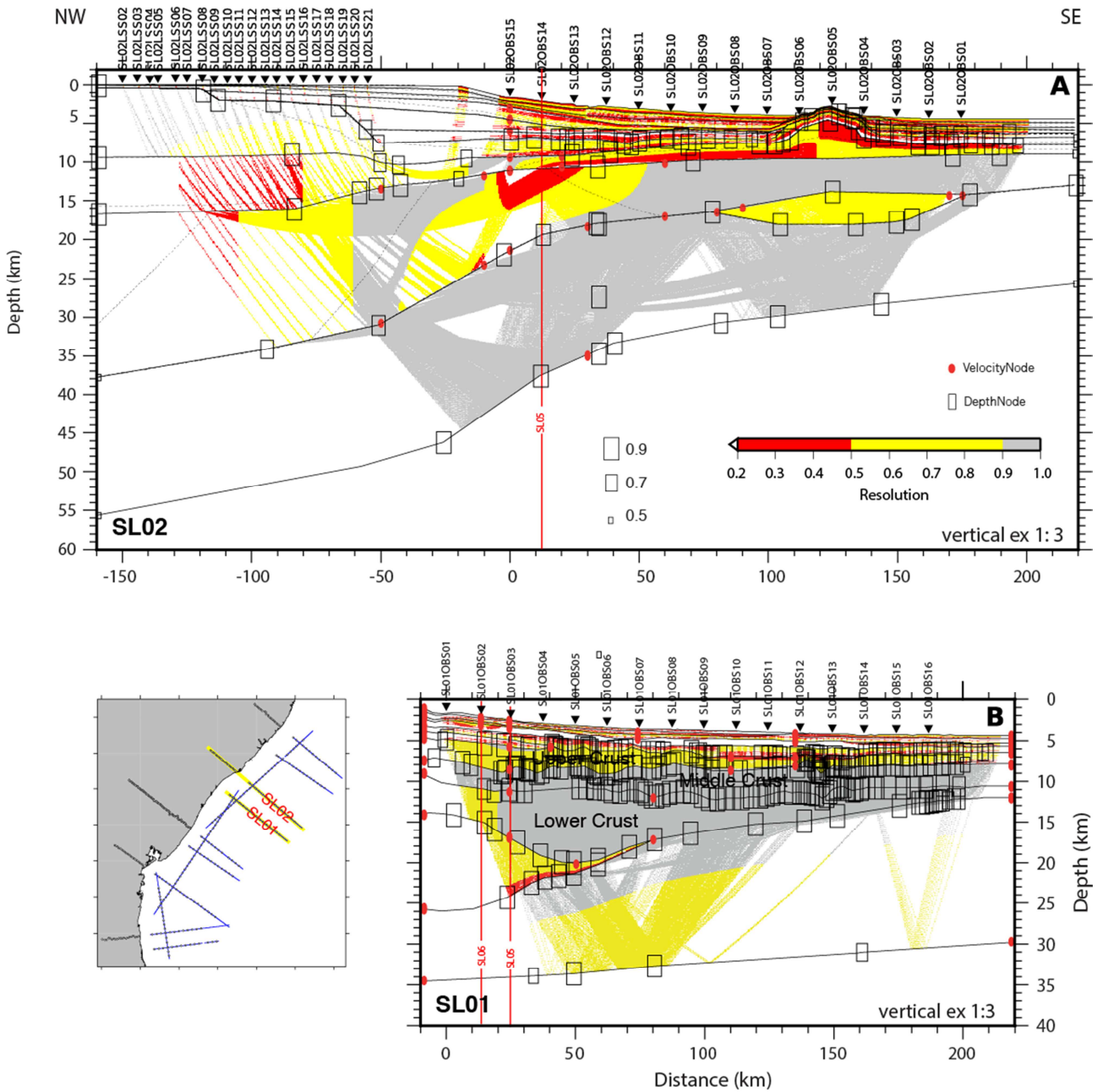
459 **Figure 12:** Gravity modeling along SL02 profile. a) Density model up to a depth of 40 km overlain by interfaces from  
460 wide-angle modeling. b) Free-air gravity anomaly observed (Pavlis et al., 2012 for the offshore data and BGI:  
461 International Gravimetric Bureau, for the land data) along the SL02 profile (red crosses) and laterally 10, 20 and 30  
462 km (SW-ward as yellow lines, NE-ward as cyan lines), measured during the SALSA experiment (blue line) and  
463 calculated (green line). Gravity modeling along SL01 profile. c) Density model up to a depth of 40 km overlain by  
464 interfaces from wide-angle modeling. d) Free-air gravity anomaly observed (Pavlis et al., 2012) along the SL01 profile  
465 (red crosses) and laterally 10, 20 and 30 km (SW-ward as yellow lines, NE-ward as cyan lines), measured during the  
466 SALSA experiment (blue line) and calculated (green line).

467

## 468 **Hitcount, spread, and resolution**

469 Interface depth node spacing as well as velocity node spacing is key to model the lateral variations  
470 of the seismic velocity with sufficient resolution, but without introducing spurious and unwarranted  
471 complexity. Although all synthetic section correctly reproduces the observed amplitude on the  
472 wide-angle data (Figures 5 to 11), suggesting a good parameterization of the model, we perform  
473 evaluation tests of the P-wave velocity models: hitcount, Spread Point Function (SPF) and  
474 resolution (Figure 13).

475 The interface nodes are spaced at less than 2 km on the seafloor where depth is well constrained by  
476 multi-beam bathymetry. Node spacing increases to 2.5 km for the three first sedimentary layers then  
477 5 km for the deepest sedimentary layers and the basement where the interface geometry is well  
478 constrained in twt from the MCS data, then 10 km for the middle crust, 15 km for the lower crust  
479 and Moho, 30 km and 50 km for the intra-mantellic reflectors. The velocity nodes are not spaced  
480 evenly but located where velocity changes are warranted by the observed wide-angle records,  
481 resulting in node spacing ranging from 30 to 350 km. The total standard deviation for depth nodes  
482 and velocity nodes is 6.229 km and 1.785 km/s, respectively. Most interface and velocity nodes in  
483 our experiment produce a hit-count larger than 3000 rays (Figure 13) with exception of the edges of  
484 our survey and the middle crust. The Spread Point Function (Figure 13) is indicative for a given  
485 velocity variation of the resulting travel-time variations when taking the different ray paths into  
486 account. Depth and velocity node SPF is relatively homogeneous in the models except in the lower  
487 crust along SL02 profile in the transition of the continental to the presumed oceanic domain.  
488 Finally, the diagonal terms of the resolution matrix are a measurement of the spatial averaging of  
489 the true earth structure by a linear combination of model parameters (Zelt 1999). Typically,  
490 resolution matrix diagonals greater than 0.5–0.7 are said to indicate reasonably well-resolved model  
491 parameters (e.g. Lutter and Nowack 1990). The major part of the interface and velocity nodes  
492 present good resolution ( $>0.7$ ). Resolution is poorest at the transition zone, in the lower crust, in the  
493 upper crust at the SAB, and under the volcanic edifice (Figure 13).



494

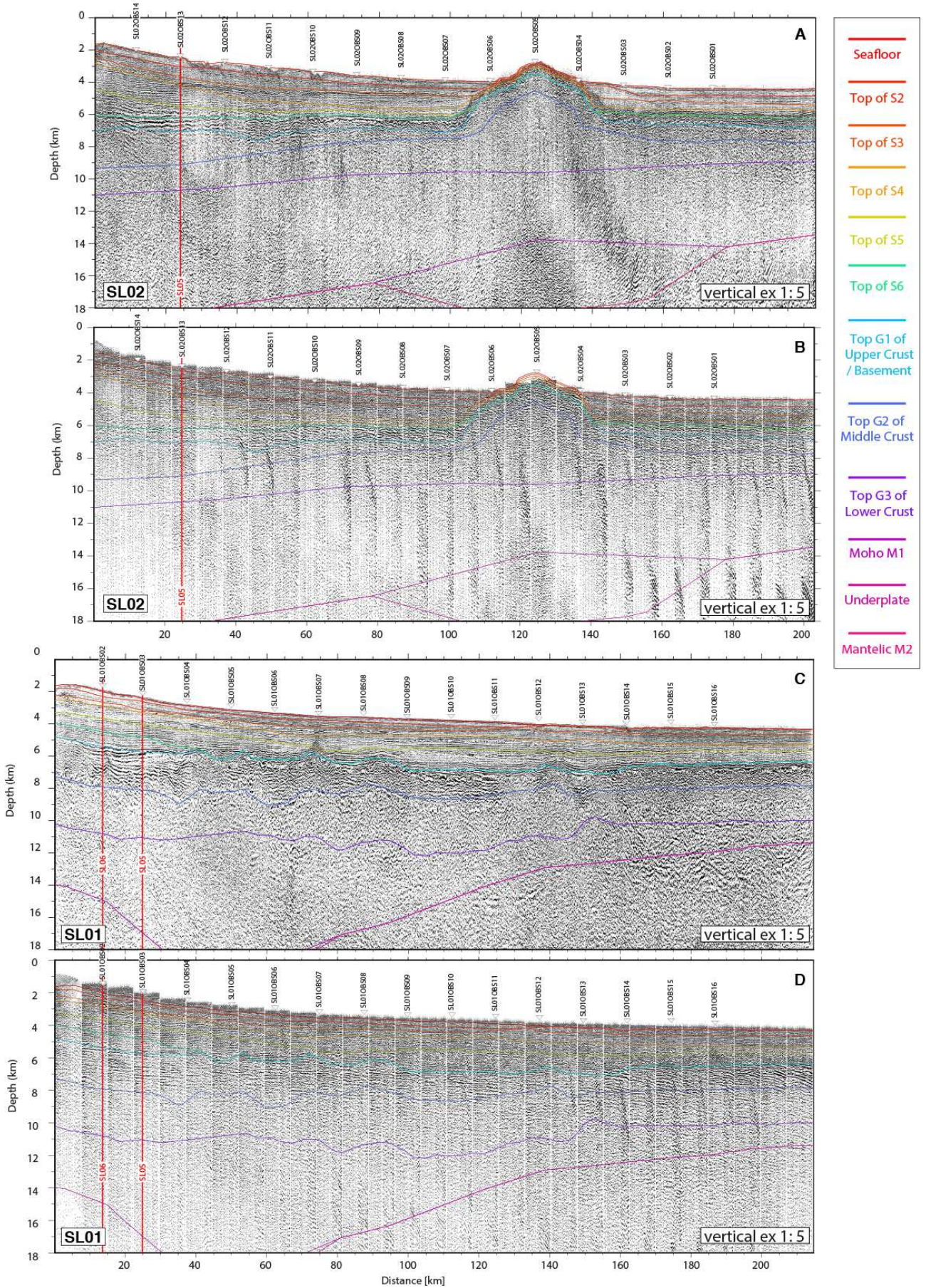
495 *Figure 13: Evaluation of the wide-angle models SL01 (A) and SL02 (B): Resolution of velocity (gridded and colored).*496 *There are zones that were not imaged due to the lack of ray coverage.*497 **MCS data pre-stack depth migration (PSDM)**

498 To verify the accuracy of the wide-angle velocity model, the MCS data is pre-stack depth migrated  
 499 and residual move-out analysis is performed. The pre-processing sequence is identical to the MCS  
 500 data time processing, and includes geometry, wave-equation multiple attenuation, shot-gather  
 501 predictive deconvolution, time variant band-pass filter, and random multiple attenuation. The  
 502 PSDM processing is undertaken using the Seismic Unix package (Stockwell Jr., 1999; Cohen and  
 503 Stockwell Jr., 2010). The PSDM consists in 2 steps: ray tracing and seismic data depth migration.

504 First, the velocity model is utilized to compute travel-time tables regularly spaced at 150 m along  
505 the profile by paraxial ray tracing on a  $50 \times 25$  m spaced grid, then travel-times in shadow zones are  
506 compensated by solving the eikonal equation. Secondly, common offset Kirchhoff depth migration  
507 is performed: Migrated traces are output as common image gathers (CIG) binned at 25 m with 30  
508 offset-classes between 249 and 4596 m at 150 m spacing. Dip-independent velocity analysis can  
509 then be performed on the migrated CIG by analyzing residual move-out. Hence, if the velocity  
510 model used for migration is close to the true medium velocity, all common offset migrated panels  
511 map the recorded seismic events to the same reflector depth, else the move-out from near to far  
512 offset translates into an interval velocity correction (Liu and Bleistein, 1995). Figure 14 presents the  
513 PSDM section and CIG gathers extracted every 7.5 km along the two profiles. Moreover, depth  
514 migrated gathers are excellent records of amplitude variations with offset (AVO), and therefore are  
515 indicators of in-situ rheological changes. The residual move-out behavior together with the seismic  
516 character from PSDM images are key elements to locate accurately major geological contacts,  
517 moreover with higher horizontal resolution when compared to the OBS records.

518 SALSA01 (Fig. 14C) and SALSA02 (Fig. 14A) were migrated up to a depth of 18 km, showing  
519 very good resolution in the sedimentary layers, and a good resolution in the crust, with good  
520 agreement between strong reflectors and their wide-angle estimated depths. The SAB shows a  
521 sedimentary structuration that can be subdivided between upper and lower packages. Upper  
522 sediments represent the first 4 layers, which are finely stratified and made of low amplitude  
523 continuous reflectors while deeper reflectors have a stronger amplitude character. The entire  
524 sedimentary package is clearly interrupted by the volcanic edifice. The upper package varies in  
525 thickness from about 1.5 km at the continental slope, 3 km at NW side of the volcano and 2 km at  
526 SE side, at the presumed oceanic basin. The lowest sedimentary package is composed by 2 layers  
527 that merge into 1 layer, at 40 km model distance on SL01, and at the NW side of the volcano at  
528 SL02. The top of this package shows the strongest and most continuous reflector in the MCS data.  
529 This reflector represents the base of the Calumbi Formation. A recede at the sea level in the end of  
530 the Coniacian controlled the erosion of the underlying sequences. This regional erosional event is  
531 represented by the so called Pre-Calumbi Formation (probably Santonian, ~86 Ma) unconformity at  
532 the base of the Piaçabuçu Group (Mohriak *et al.*, 1998; Campos Neto *et al.*, 2007). This  
533 unconformity can be observed as the most remarkable reflector, and is interpreted as a regional  
534 angular, intra-Cretaceous unconformity in the platform that is almost flat-lying in the deep-water  
535 region and overlies horizontal sedimentary layers (Mohriak *et al.*, 1998, 2000).

536 The basement is composed by chaotic seismic facies in the MCS data. Below the basement it is  
537 impossible to differentiate any seismic facies or structure. Unlike the profile SL01 (Figure 4), no  
538 reflector corresponding to the Moho is observed in the profile SL02.



540

541

542

Figure 14: a) Pre-stack depth migrated record section of MCS data along SL02 profile. Model's interfaces are represented with continuous lines. The intersections with the SALSA dataset are indicated by red line. Vertical

543 *exaggeration is 1:5. b) Residual move-out of MCS data along SL02 profile. Common image gathers are spaced every*  
544 *7.5 km. c) Pre-stack depth migrated record section of MCS data along SL01 profile. Vertical exaggeration is 1:5. b)*  
545 *Residual move-out of MCS data along SL01 profile. Common image gathers are spaced every 7.5 km. Vertical*  
546 *exaggeration is 1:5.*

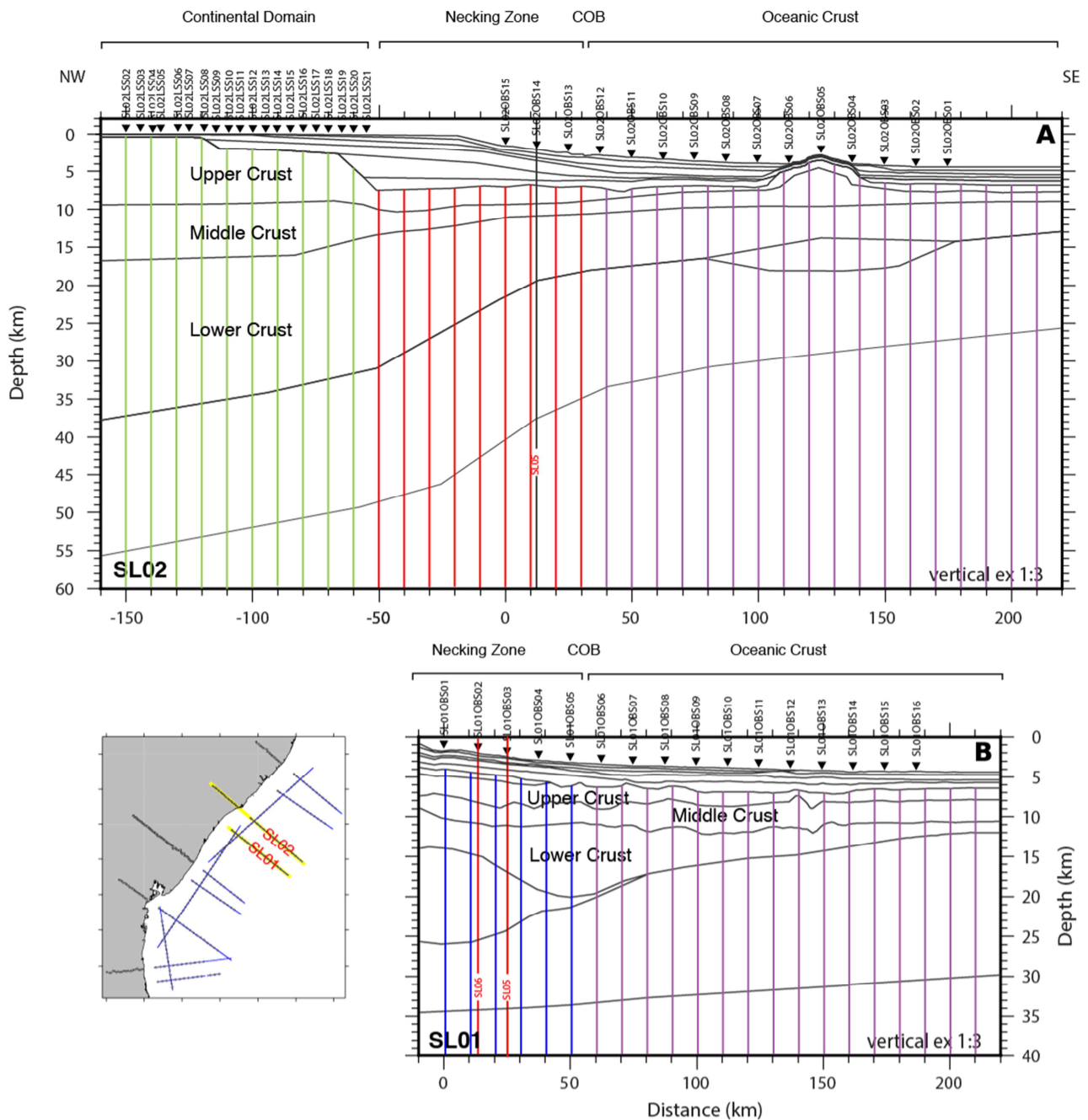
547

## 548 Discussion

549 In order to constrain the nature of the crust, 1D crustal velocity- depth ( $V_z$ ) profiles were extracted  
550 underneath the top of the basement at a 10 km interval from the final velocity models (Figure 15).  
551 These  $V_z$  graphs can be compared to compilations for typical continental crust (Christensen and  
552 Mooney, 1995) and Atlantic-type oceanic crust (White *et al.*, 1992) that allow to discuss the  
553 properties of crust and to establish the lateral segmentation along the profiles.  
554 On the base of this analysis of the final models and these  $V_z$  graphs, three distinct domains can be  
555 distinguished: 1. Unthinned Continental Domain; 2. a domain of crustal thinning, the Necking  
556 Domain; and lastly, 3. an external distal domain interpreted to be of oceanic nature (Figure 15). No  
557 transitional domain is defined in the SAB, the transition between the thinned continental and  
558 oceanic crusts is direct.

559

560



561  
 562 Figure 15: Distribution of 1-D velocity profiles extracted from the final P-wave interval velocity model and color coded  
 563 according to segmentation along the SL02 (A) and SL01 (B) profiles

## 564 Unthinned Continental Domain

565 This domain is essentially based on the profile SL02 data, taking into consideration that it is the  
 566 unique profile with landstations.

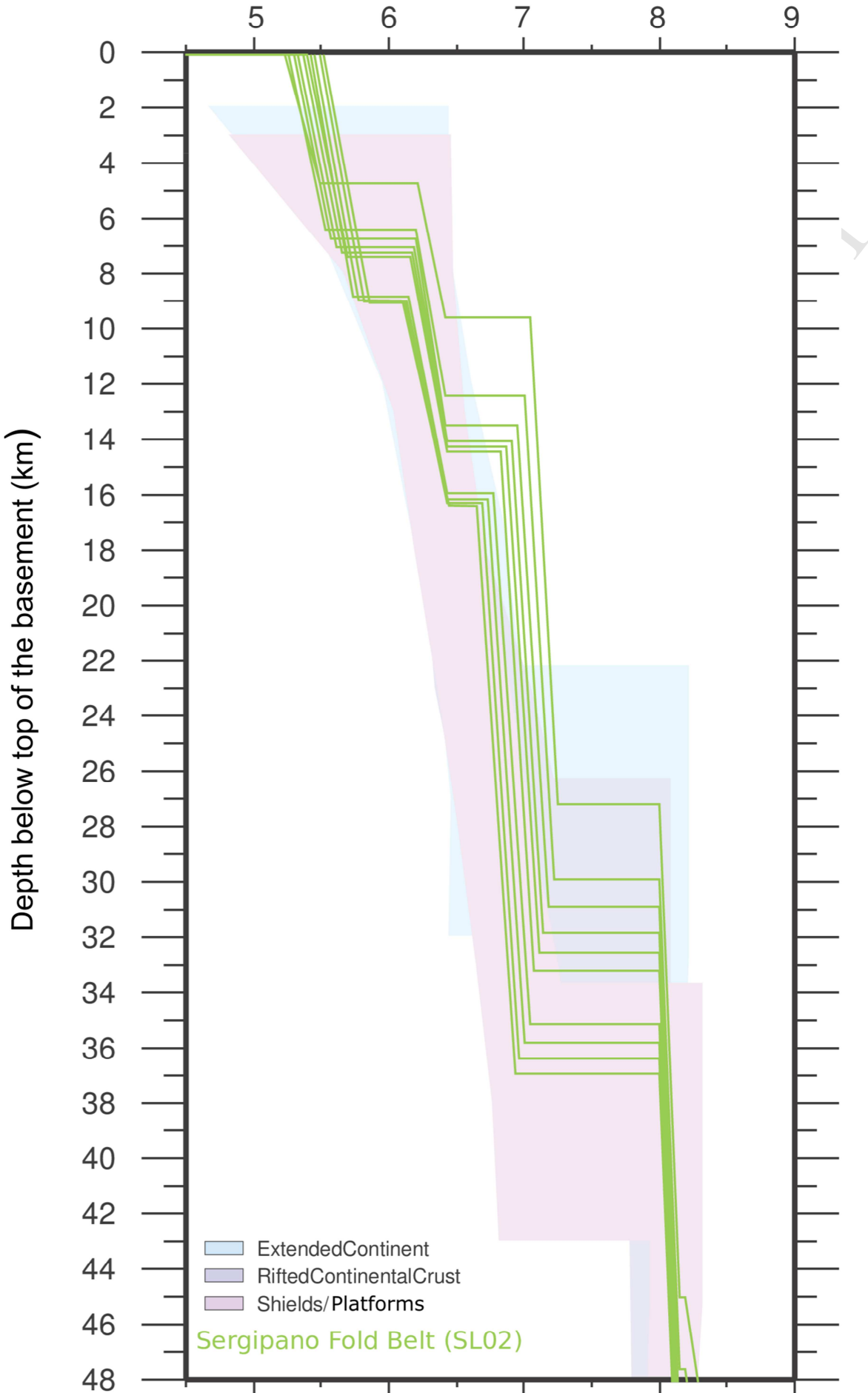
567 As the inland proximal part of the profile, between the landstations and the OBSs, is not completely  
 568 constrained by the seismic rays, the modeling of the Unthinned Continental domain, was also  
 569 constrained by additional information obtained from the crossing with profile SL05 (Evain, *et al.*, In

570 prep.), and bibliographical information (Chang *et al.*, 1992 ; Feijó *et al.*, 1994 ; Mohriak *et al.*,  
571 1995, 1998, 2000; Blaich *et al.*, 2008 ; Soares *et al.*, 2010 ; Tavares *et al.*, 2012 ; de Lima *et al.*,  
572 2015) .

573 In the Continental domain, the Moho is 27 to 37 km depth below basement (Figure 16). The  
574 comparison of the 1D velocity profiles with a worldwide compilation of the continental crust  
575 (Christensen and Mooney, 1995) clearly shows similarities both in velocities and gradients with our  
576 results (Figure 16).

ACCEPTED MANUSCRIPT

Velocity (km/s)



578 *Figure 16: Compilation of 1D velocity-depth profiles extracted below the top of the basement ( $V_z$ ) in the domains of*  
579 *unthinned continental crust. The light blue areas correspond to averaged velocity profiles for continental crust*  
580 *(Christensen and Mooney, 1995).*

581

582 At the SL02 profile, in the Continental domain, the top of the upper crust, the basement, is at the  
583 surface until -120 km distance model, then it deepens, forming three “stairs”, first at -120 km  
584 distance model, where it deepens to 2.5 km deep, and then at -60 km distance model it deepens to 8  
585 km deep (Figures 15 and 16). The upper layer has velocities between 5.50 and 5.90 km/s, that  
586 decreases seawards. The topography of the interface between the upper and middle crust is almost  
587 regular for all along the profile, and the velocities of the middle crust range from 6.10 to 6.50 km/s.  
588 The base of the lower crust corresponds to the Moho, whose depth decreases smoothly from 37 to  
589 33 km. Its velocities at the top increase from 6.60 km/s in most continental part, to 7.30 km/s  
590 seawards, near to the Necking Zone and its velocities at the base, range from 6.90 km/s at the  
591 continental domain to 7.50 km/s near the Necking Zone.

592 The deep seismic refraction experiment carried out in the Pernambuco Province, northwards (Figure  
593 1) (Soares *et al.*, 2010; Tavares *et al.*, 2012; Lima *et al.*, 2015) shows a structure of the lithosphere,  
594 with 2 layers separated at about 16 km depth, with a velocity of 5.75 to 6 km/s at the top and 6.2 to  
595 6.3 km/s at the base of the upper crust, and 6.4 to 6.5 km/s at the top and 6.75 to 6.90 km/s at the  
596 base of the lower crust, for a total continental crust thickness of about 32 km. In terms of velocities,  
597 this structure is quite similar to that found in SL01 and SL02. The upper layer found by these  
598 authors, would correspond to the upper and middle layer of SL01 and SL02.

599 These similarities put into question the proposition that the SFB is a Neoproterozoic fold–thrust belt  
600 produced by inversion of a passive margin basin located at the northeastern edge of the ancient Sao  
601 Francisco plate (Almeida *et al.*, 1977 ; D’el-Rey Silva, 1999) and constituted by a 42 km thick crust  
602 (Oliveira *et al.*, 2008) and reinforces the idea that the SFB was possibly on the margin of the  
603 Palaeoproterozoic Pernambuco–Alagoas Block (Oliveira *et al.*, 2010), and was attached to the Sao  
604 Francisco Craton during the Brasiliano (~600 Ma) orogenic event (Davison and Santos, 1989; Silva  
605 Filho, 1998). These results put the limit clearly between the Sao Francisco Craton and the  
606 Palaeoproterozoic Pernambuco–Alagoas Block on the Vaza Barris transfer zone, considering it as a  
607 major structural fault.

### 608 **Necking Zone:**

609 The necking zone goes from -55 km to 25 km profile distance. On profile SL02, throughout the  
610 necking zone, the total crustal thickness, without the water column (~4 km through the COB) and

611 sediment cover, thins from ~23 km to ~10 km. The thickness of the upper crust thins from 10 km in  
612 the limit with the continental domain to only 1 to 2 km seaward in the limit with the oceanic  
613 domain. At the depocenter of the SAB, at -50 km distance of the profile, the top of the upper crustal  
614 layer deepens to ~8 km and remains at this depth for all along the profile. The thickness of the  
615 middle crust thins from ~7 km in the limit with the continental domain, to ~2 km through the  
616 necking domain until the COB. The Moho rises from 31 km depth in the limit with the continental  
617 domain to ~18 km depth in the COB over a distance of almost 100 km (Figure 8), and the total  
618 thickness of the lower crust thins from 19 km in limit with the continental domain to 8 km beneath  
619 the COB, with a light velocity increase in the middle of the Necking Zone. The lateral velocity  
620 change happens only in the lower crust where it changes from 7.0 to 7.3 km/s on the top and from  
621 7.25 to 7.5 km/s at the base. In the Necking Zone between 30 and 90 km distance, and 9 and 15 km  
622 depth, there are also packages of intra-crustal reflectors that may correspond to SDRs. Although the  
623 base of the crust is much clearer in SL02 than in SL01, without basal intra-crustal reflectors.

624 The gravity data shows a prominent positive anomaly in the necking zone.

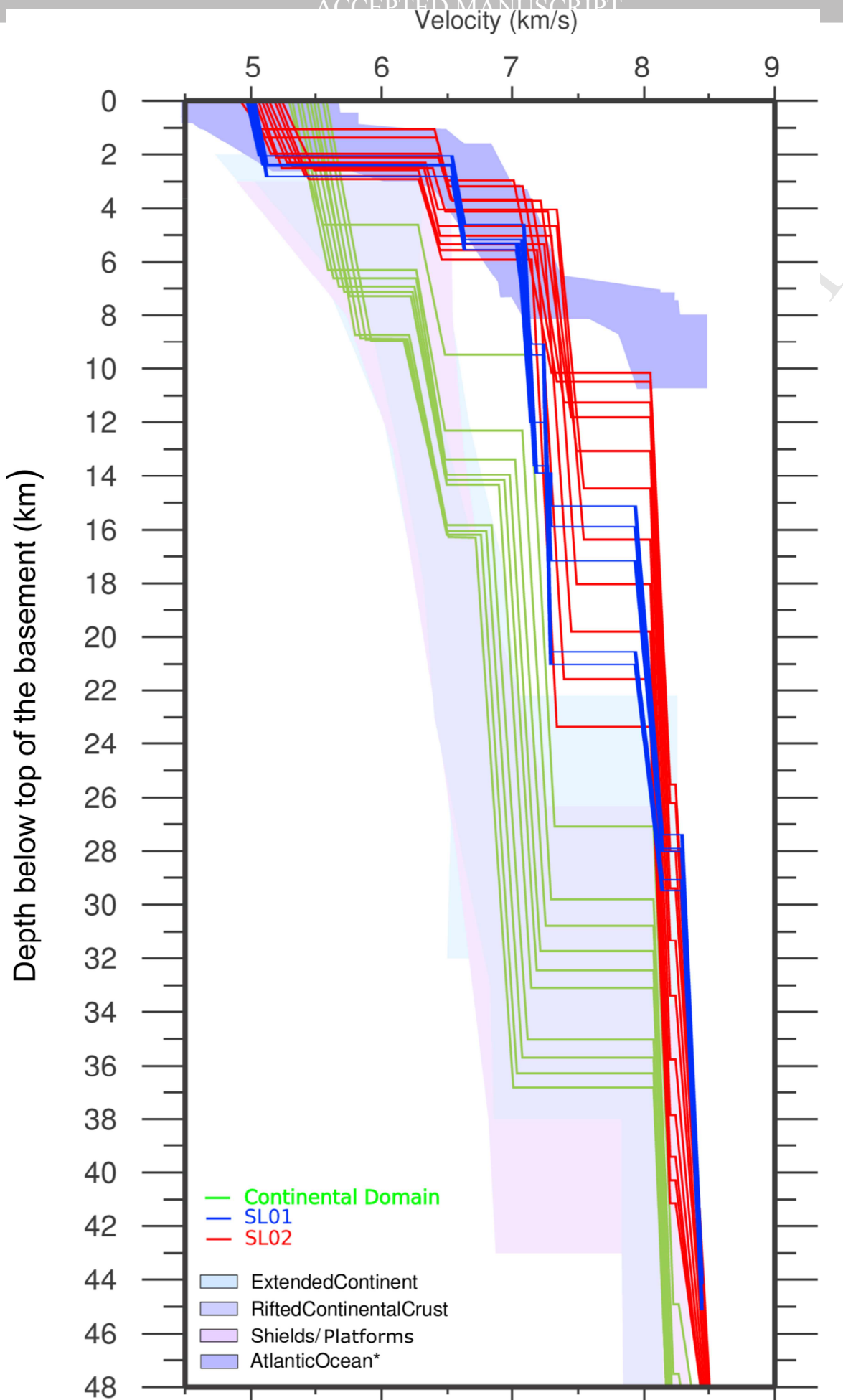
625 The necking zone of the SL01 is partially constrained in the wide-angle data (Figures 8 and  
626 15), but in the MCS (Figures 4 and 14), it presents a zone of intracrustal reflectors between 4 and 8  
627 km depth and between 10 and 70 km model distance. We can recognize few SDRs pattern in this  
628 zone, and, in the GXT-ION profiles, a group of deeper reflectors in the lower crust, near the Moho  
629 discontinuity, between 20 and 25 km depth, and between 20 and 80 km model distance. These  
630 reflectors were interpreted by Mohriak *et al.* (1998) as a gradational passage from the lower crust to  
631 the lithospheric mantle. In this same zone, we observe a very irregular topography in the basement,  
632 showing some structures that look like volcanic plugs (Mohriak *et al.*, 1995, 1998).

633 This zone gives a chaotic response in the wide-angle data. Additionally, the fact that this area  
634 is a zone with poor data coverage and no inland continuation makes difficult a detailed  
635 interpretation of the crustal framework near the base of the crust. However, in wide-angle data, the  
636 Pmp is very clear and allows us to make a good interpretation of the Moho discontinuity. It rises  
637 from 25 km depth in the extreme NW of the profile to 18 km in the transition of the continental to  
638 oceanic crust at ~70 km distance in the profile (Figure 8). In the lower crust, the array of basal intra-  
639 crustal reflectors is disposed in an anticlinal pattern that gives an idea of a lenticular shape (figure  
640 8). In this zone, the velocity goes from 7.0 to 7.3 km/s laterally. Loureiro *et al.* (2018) found some  
641 similar structures in the profile SL11, located at the Jequitinhonha basin, near a zone of “necking  
642 zone wideness” transition.

643 Buck (1991, 1999) reports “a series of basins and ranges in a broad region of continental  
644 extension”. According to Buck (1999), this pattern, is related to lateral periodic variations in the rate

645 of extension, which causes the so-called “lithospheric *boudinage*”. This process of *boudinage* of the  
646 lithosphere produces variations on the local isostasy, also called crustal buoyancy (Block and  
647 Royden, 1990; Bird, 1991; Buck, 1991, 1999).

648 From the Continental Domain to seawards, the total crustal thickness, without the water  
649 column (~4 km through the COB) and sediment cover, thins from ~33 km at the most continental  
650 part, to ~10 km through the COB and the change in the velocity of the lower crust may therefore be  
651 interpreted as a density compensation to effect of *boudinage* process and/or as volcanic intrusions.



653 *Figure 17: Compilation of 1D velocity-depth profiles extracted below the top of the basement ( $V_z$ ) in the Unthinned*  
654 *Continental Domain (green lines) and the Necking Zone (red and blue lines). The blue shaded area bounds a*  
655 *compilation of velocity profiles for typical Atlantic oceanic crust (White *et al.*, 1992), and light blue areas correspond*  
656 *to averaged velocity profiles for continental crust (Christensen and Mooney, 1995).*

657

658 Figure 17 shows that the transition between the unthinned continental crust and the thinned domain  
659 preserves the configuration and the velocities of the crustal layers with strong velocity steps. The  
660 total crustal thickness has a sharp transition and the comparison of the  $V_z$  of the two profiles with  
661 the compilations for a typical continental crust (Christensen and Mooney, 1995) and for Atlantic-  
662 type oceanic crust (White *et al.*, 1992), shows that the crustal nature in the necking zone is closer to  
663 a typical continental crust than a typical oceanic crust (Figure 17). We propose that the necking  
664 seems therefore to be constituted by thinned continental crust, that presents a continuity of the  
665 velocity structure during the thinning process, without the presence of a transitional crust, and the  
666 main change to oceanic crust occurs outside the Necking Zone.

### 667 **Oceanic domain:**

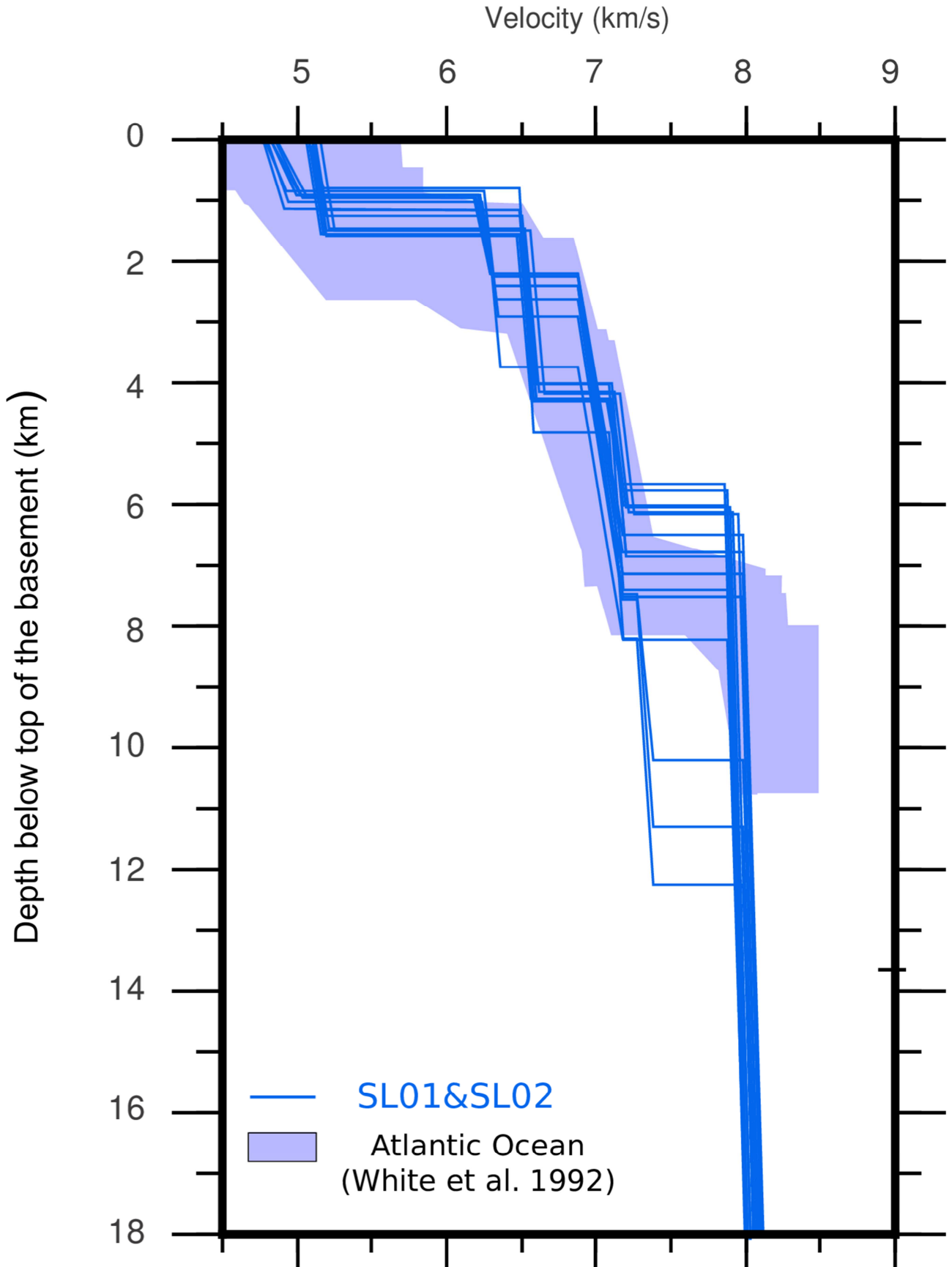
668 The External Domains (25-210 km distance model on SL02 and 70-210 on SL01) show a thinner  
669 crustal thickness and is interpreted as formed by oceanic crust. The sedimentary cover is also  
670 thinner and reaches 3 km. The top of the basement located at 6-8 km depth assumes a much more  
671 regular topography. The crustal layers do not present any significant lateral velocity gradient  
672 through the transition from continental to oceanic crust. Figures 15 and 18 show that, except under  
673 the volcanic edifice, where the top of the basement follows the topography of the volcano, the  
674 average depth of the oceanic basement varies between 6 to 8 km (Figure 8).

675 Due to the fact that this crust was formed during the Cretaceous Normal Superchron (CNS), a  
676 magnetic quiet period, it presents a lack of reversal-related magnetic anomalies on crust of age 121  
677 (Anomaly M0y) to 83.6 (Anomaly C34y) Ma old (Malinverno *et al.*, 2012; Ogg, 2012; Granot *et*  
678 *al.*, 2014).

679 Nevertheless, the  $V_z$  profiles (Figure 18) along the profiles SL01 and SL02 show that the oceanic  
680 basement and its layers fit almost perfectly the worldwide compilation for Atlantic-type oceanic  
681 crust (White *et al.*, 1992). The Moho has a range of depths below basement that varies from 6 to 12  
682 km. It slightly rises from NW to SE in the proximal part of the oceanic domain (Figure 18), of the  
683 closest to the transition with continental crust, and deepens under the volcanic edifice along SL02  
684 profile. The rest of the oceanic crust thickness ranges from 8 to 6 km (Figure 18). Larger Moho  
685 depths under the volcano can be justified due to the presence of the undercrustal layer that reflects

686 isostasy compensation. Despite the thick crust in this area, crustal velocities go according with the  
687 compilation of a typical oceanic crust (White *et al.*, 1992).

ACCEPTED MANUSCRIPT



689 *Figure: 18 Compilation of 1D velocity-depth profiles extracted below the top of the basement ( $V_z$ ) in the proposed*  
690 *Oceanic Crust. Colored lines mark individual  $V_z$  profiles at a 10 km interval of profiles SL01 and SL02. The blue*  
691 *shaded area bounds a compilation of velocity profiles for typical Atlantic oceanic crust (White et al., 1992).*

692 The figure 8 shows a comparison between the data and the segmentation obtained in this work and a  
693 line-drawing of the ION-GXT seismic profiles. The wide-angle models go mostly in accord with  
694 the crustal structures interpreted from the ION-GXT lines, except for the Moho along SL01 which  
695 is modeled on average 2 km shallower with wide-angle data than the deepest reflector seen on the  
696 depth converted MCS line.

697

698

## 699 **Continental-Oceanic Boundary**

700 The transition between the continental and the oceanic domain is characterized in the MCS  
701 profiles (Figures 4 and 14) by a zone dominated by intracrustal reflectors. These reflectors in most  
702 part look like SDRs, but there is also some that are similar to LDRs. At this zone, the basement  
703 topography shows some mounds and little elevations. All these structures could be classified as a  
704 magmatic signature. Notwithstanding that, as Moulin *et al.* (2005) noticed already, these structures  
705 are not sufficient to characterize an archetype that could classify the margin of the SAB as a  
706 volcanic margin similar to the Greenland or Argentina Margins. Moreover, there is no evidence in  
707 the bibliography of volcanism before the first production of ocean crust. As described by Mohriak  
708 *et al.* (1998), these magmatic features are probably associated with extensional processes and  
709 oceanic crust inception, and they apparently post-date the rift phase lithospheric extension  
710 associated with the breakup of Gondwana in the Early Cretaceous, and were used by Mohriak *et al.*  
711 (1995, 1998) and Blaich *et al.* (2008) for their localization of the COB. Based on our wide-angle  
712 data analysis, we pointed the COB at ~70 km from the coast, between the SL02OBS13 and  
713 SL02OBS12 along the SL02 profile just seaward of the slight velocity increase in the lower crust,  
714 and ~100 km from the coast, between the SL01OBS05 and the SL01OBS06, along the SL01 profile  
715 just seaward of the intra-crustal velocity body, a little further seaward than the COB pointed by  
716 these authors.

717

## 718 **Conclusions**

719 The P-wave modelling of the SL01 and SL02 profiles reveals the deep crustal structure of  
720 the SAB passive margin off NE Brazil. From these models, we conclude that:

- 721 • The SAB margin is segmented parallel to the NE-SW coastline and the hinge line of  
722 the platform into a Continental Domain, a Necking Zone and an Oceanic Crust Domains without  
723 transitional domain.
- 724 • The oceanic crust is therefore rapidly reached, less than 100 km from the coast; its  
725 limit is parallel to the coast all along this segment. The COB is therefore situated a little further  
726 seaward than pointed out by Mohriak *et al.* (1995, 1998) and Blaich *et al.* (2008).
- 727 • These results show the huge segmentation in the offshore deep structures of the NE  
728 Brazilian margins since as opposed to this study a wide transitional domain of exhumed lower  
729 continental crust is imaged 350 km southwards in the Jequitinhonha margin (Loureiro *et al.*, 2018).
- 730 • Onshore, LSS data along SL02 profile allow the characterization of the unthinned  
731 continental crust. It is ~30–35 km thick, divided into three layers with velocities between 5.0 and  
732 7.2 km/s. The results confirm the general trend modelled by previous studies of Mohriak *et al.*  
733 (1995, 1998); Blaich *et al.* (2008).
- 734 • The Necking Zone presents a rather sharp crustal thinning on the north of the Vaza-  
735 Barris fault (SL02), where the Moho goes from 31 km to 18 km depth in less than 100 km, and the  
736 first thinning corresponds to the vanishing of the upper crust, that thins from 10 km, at the  
737 continental domain, to less than 2 km through the COB, and keeps this thickness seawards. The  
738 Moho rises from a depth of 33 km at the limit with Continental Domain to a depth of 16 km through  
739 the COB. The lateral velocity variation happens only in the lower crust where it goes from 7.0 to  
740 7.3 km/s at the top and from 7.25 to 7.5 km/s at the base. This wide-angle model shows a Moho  
741 located slightly (2 km) shallower than the one found by Mohriak *et al.* (1998) and confirms the  
742 gravity model of Blaich *et al.* (2008).
- 743 • Further SE, a 9 km thick typical oceanic crust is present, with a thin upper layer (1–  
744 1.5 km) that presents velocities varying from 5.0 to 5.20 km/s, a 2.5 km thick middle layer with  
745 velocities of 6.5–6.6 km/s, and a thicker lower layer with 3-4 km thick and 6.9 to 7.1 km/s. The  
746 transition between the necking zone and this domain is characterized by a zone dominated by  
747 intracrustal reflectors, which could reflect a magmatic signature, notwithstanding that, as Moulin *et*  
748 *al.* (2005) noticed already, these structures are not sufficient to characterize an archetype that could  
749 classify the margin of the SAB as a volcanic margin. As described by Mohriak *et al.* (1998), these  
750 magmatic features are associated with extensional processes and oceanic crust inception, and they  
751 apparently post-date the rift phase lithospheric extension associated with the breakup of Gondwana  
752 in the Early Cretaceous.

753 • This oceanic crust is affected on profile SL02 by a volcanic edifice with 40 km  
754 extension where the basement rises almost 4 km. The Bahia Seamounts chain has U/Pb ages from  
755 75 to 84 Ma and is supposed to be related to a post-rift hotspot localized near the Middle Atlantic  
756 Ridge (MAR) (Skolotonev, 2012). Below this domain, there is a sub-crustal layer, very well  
757 constrained by the OBS and gravity data, with ~5 km thick and 7.3 km/s velocity. This layer is  
758 probably related to a magmatic underplating process where basaltic magmas are frequently trapped  
759 at or near the Moho, or within the crust, or in complex crust-mantle transition zones (Cox,1993).

760 • The undulated intracrustal reflectors, with an anticlinal shape, in the base of the  
761 lower crust of the necking zone in SL01 profile, added to the rise in the seismic velocity are a good  
762 evidence that the rift caused a lithospheric boudinage. This zone of boudinage is near of and is  
763 probably affected by the Vaza-Barris Transfer Zone. A similar feature is observed further in the  
764 south, at the Jequitinhonha Basin (Loureiro *et al.*, 2018), where the crust is also affected by  
765 boudinage, near a zone of “necking zone wideness” transition. Buck *et al.* (1999) proposed that  
766 lithospheric boudinage is formed under local isostatic effect, sometimes called crustal buoyancy.  
767 Due to a possible heterogeneity, the crust was affected by a non-homogeneous thinning and  
768 extension, generating crustal boudinage. It can be explained by some transformations in the  
769 composition of the lower crust under the necking. On the other hand, this boudinage could be a  
770 consequence of magmatic intrusions formed during the rift process. However, the Pmp in the wide-  
771 angle data, is clear and continuous, and do not seem to have been influenced by a volcanic  
772 intrusion.

773 • The SFB, which was in the margin of the Pernambuco Alagoas Domain, and was  
774 formed by thrust faulting of this domain over the São Francisco Craton during the Brasiliano  
775 orogeny, resulting in the collage of its crusts (Oliveira *et al.*, 2010). The comparison between  
776 velocity models of the Pernambuco Alagoas Domain (Soares *et al.*, 2010; Tavares *et al.*, 2012; de  
777 Lima *et al.*, 2015) and the São Francisco Domain (Soares *et al.*, 2006 and Soares, personal  
778 communication), shows that the crust in the SFB is much more similar to the Pernambuco Alagoas  
779 Domain than to the São Francisco Craton. This could mean that the São Francisco crust was  
780 subducted and consumed, and the crust of the Pernambuco-Alagoas predominated in the Brasiliano  
781 orogenic event as it was proposed by Oliveira *et al.* (2010).

782

### 783 **Contributions**

784 The SALSA Project was led by D. Aslanian and M. Moulin, from Ifremer, and A. Viana and J. A.  
785 Cupertino, from Petrobras. Modeling of the SALSA profile was done by M. Evain, A. Afilhado, F.

786 Gallais, A. Loureiro, F. Schnurle and F. Klingelhofer. On-land operation was conducted by J.  
787 Soares, R. Fuck, M. Vinicius de Lima, from the University of Brasilia (UnB) L. Matias, and C.  
788 Corela from the Instituto Dom Luis (IDL) of the University of Lisbon. Processing of the MCS  
789 seismic data was done by P. Schnurle. This work has been conducted as part of a PhD project  
790 supported by the Conselho Nacional de Desenvolvimento Científico e Tecnológico (CNPQ) from  
791 Brazil.

792

### 793 Acknowledgments

794 The data set collected during the SALSA experiment is protected under a partnership between  
795 IFREMER and Petrobras. Any request has to be addressed to Daniel Aslanian (aslanian@ifremer.fr)  
796 and Adriano Viana (aviana@petrobras.com.br). The authors wish to thank the captain, crew, and  
797 MCS technical team of the French R/V L'Atalante. Many thanks also to the OBS and land station  
798 technical teams who made this experiment possible. The GMT [Wessel and Smith, 1998], Seismic  
799 Unix software package [Stockwell, 1999], GEOCLUSTER software (CGG-Veritas), and  
800 RAYINVR software (Zelt and Smith, 1992; Zelt *et al.*, 1999) were used in the preparation of this  
801 paper. The Salsa Team is composed by: Morvan, L.<sup>1</sup>; Mazé, J.P.<sup>1</sup>; Pierre, D.<sup>1</sup>; Roudaut-Pitel, M.<sup>1</sup>;  
802 Rio, I.<sup>3</sup>; Alves, D.<sup>3</sup>; Barros Junior, P.<sup>7</sup>; Biari, Y.<sup>1</sup>; Corela, C.<sup>3</sup>; Crozon, J.<sup>1</sup>; Duarte, J.L.<sup>3</sup>; Ducatel,  
803 C.<sup>1</sup>; Falcão, C.<sup>7</sup>; Fernagu, P.<sup>1</sup>; Le Piver, D.<sup>1</sup>; Mokeddem, Z.<sup>6</sup>; Pelleau, P.<sup>1</sup>; Rigoti, C.<sup>7</sup>; Roest, W.<sup>1</sup>;  
804 Roudaut, M.<sup>1</sup>.

805 We would like to thank two anonymous reviewers and the editor Dr. F. Audemard,  
806 who helped to improve significantly this manuscript.

### 807 References

- 808 Almeida F. F. M., Hasui Y., Brito Neves B.B. Fuck R.A. (1977). Províncias Estruturais  
809 Brasileiras. *In: SBG-Núcleo Nordeste, Simpósio Geologia do Nordeste*, 8, Campina Grande, *Atas*,  
810 *Boletim* 6, p. 363-391.
- 811 Austin, J. A., Jr., and Uchupi, E. (1982). Continental-oceanic crustal transition of Southwest  
812 Africa. *Am. Assoc. Petrol. Geol. Bull.*, 66, 1328±1347
- 813 Bauer, K., Neben, S., Schreckenberger, B., Emmermann, R., Hinz, K., Fechner, N., Gohl, K.,  
814 Schulze, A., Trumbull, R. B., Weber, K. (2000). Deep structure of the Namibia continental margin  
815 as derived from integrated geophysical studies. *Journal of Geophysical Research: Solid*  
816 *Earth*, 105(B11), 25829-25853.
- 817 Blaich, O.A., Tsikalas, F., Faleide, J.I. (2008). Northeastern Brazilian margin: regional  
818 tectonic evolution based on integrated analysis of seismic reflection and potential field data and  
819 modelling. *Tectonophysics*, 458: p.51-67.
- 820 Blaich, O.A., Faleide, J.I. Tsikalas, F. 2011. Crustal breakup and continent-ocean transition  
821 at South Atlantic conjugate margins. *Journal of Geophysical Research*, 116, B01402,  
822 doi:10.1029/2010JB007686.

- 823 Black, R., and Girod, M. (1970). Late Paleozoic to Recent igneous activity in West Africa and  
824 its relationship to basement structure. *African magmatism and tectonics*, 1(8), 5-2.
- 825 Bonatti, E. (1996). Anomalous opening of the Equatorial Atlantic due to an equatorial mantle  
826 thermal minimum. *Earth and Planetary Science Letters*, 143: 147-170.
- 827 Buck, W. R., Lavier, L. L., Poliakov, A. N. (1999). How to make a rift wide. *Philosophical*  
828 *Transactions-Royal Society of London Series a Mathematical Physical and Engineering Sciences*,  
829 671-689.
- 830 Cainelli, C. (1992). Sequence stratigraphy, canyons, and gravity mass flow deposits in the  
831 Piacabuçu Formation, Sergipe-Alagoas Basin, Brasil. *PhD thesis, University of Texas at Austin*, 233  
832 p.
- 833 Cainelli, C., and Mohriak, W. U. (1998, November). Geology of Atlantic eastern Brazilian  
834 basins. In *Brazilian Geology Part* (Vol. 2, p. 1998).
- 835 Carvalho, M. J., (2005). Tectonic Evolution of the Marancó-Poço Redondo Domain: Records  
836 of the Cariris Velhos and Brasileiro Orogenesis in the Sergipano Belt, NE Brazil. Tese de  
837 doutorado. Universidade de Campinas.
- 838 Campos Neto, O., Lima, W. S., Cruz, F. G. (2007). Bacia de Sergipe-Alagoas. *Boletim de*  
839 *Geociências da PETROBRAS*, 15(2), 405-415.
- 840 Christensen, N. I., and Mooney, W. D. (1995). Seismic velocity structure and composition of  
841 the continental crust: A global view. *Journal of Geophysical Research: Solid Earth*, 100(B6), 9761-  
842 9788. doi:10.1029/95JB00259
- 843 Cohen, J. K. and Stockwell Jr., J. W. (2010). CWP/SU: Seismic Unix Release 42: a free  
844 package for seismic research and processing, *Center for Wave Phenomena, Colorado School of*  
845 *Mines*.
- 846 Cornacchia, M., and Dars, R. (1983). Un trait structural majeur du continent Africain; les  
847 lineaments centrafricains du Cameroun au Golfe d'Aden. *Bulletin de la Société Géologique de*  
848 *France*, 7(1), 101-109.
- 849 Conceição, J.C.J., Zalán, P.V., Wolff, S. 1988. Mecanismo, Evolução e Cronologia do Rift  
850 Sul-Atlântico, *Boletim de Geociências da PETROBRAS*, 2(4):255-265
- 851 Contrucci, I., Matias, L., Moulin, M., Géli, L., Klingelhofer, F., Nouzé, H., Aslanian D.,  
852 Olivet J. L., Réhault J. P., Sibuet, J. C. (2004). Deep structure of the West African continental  
853 margin (Congo, Zaïre, Angola), between 5 S and 8 S, from reflection/refraction seismics and  
854 gravity data. *Geophysical Journal International*, 158(2), 529-553.
- 855 Davison, I. and Santos, R.A., (1989). Tectonic evolution of the Sergipano Fold Belt, NE  
856 Brazil, during the Brasileiro Orogeny. *Precamb. Res.*, 45. p. 319-342.
- 857 D'el-Rey Silva, L. J. H. (1999). Basin infilling in the southern-central part of the Sergipano  
858 Belt (NE Brazil) and implications for the evolution of Pan-African/Brasiliano cratons and  
859 Neoproterozoic sedimentary cover. *South American Journal of Earth Sciences*, 12: 453-470
- 860 Dumont, J. F. (1986). Identification par télédétection de l'accident de la Sanaga (Cameroun):  
861 Sa position dans le contexte des grands accidents d'Afrique Centrale et de la limite nord du craton  
862 Congolais. *Géodynamique*, 1(1), 13-19.
- 863 Eldholm, O., Thiede J., and Taylor E. (1989). Evolution of the Vøring volcanic margin,  
864 *Proceedings of the Ocean Drilling Program - Scientific Results*, 104, 1033-1065.
- 865 Feijó, F. J. (1994). Bacia de Sergipe-Alagoas. *Boletim de Geociências da PETROBRAS*, Rio  
866 de Janeiro, 8(1):149-161

- 867 Gomes, P. O. (2005). Tectonismo, Vulcanismo, Sedimentação e Processos erosivos No  
868 Segmento Nordeste Da Margem Continental Brasileira. *Phd thesis. Universidade Do Estado Do Rio*  
869 *De Janeiro Faculdade De Geologia*.
- 870 Humphrey, F. L.; Allard, G. O. (1969). Geologia da área do domo de Itabaiana (SE) e sua  
871 relação com a geologia do geossinclinal de Propriá – Um elemento tectônico recém-conhecido no  
872 Escudo Brasileiro. (1969). *Tradução de Munne, A. I., Barão, S. C. Rio de Janeiro,*  
873 *PETROBRAS/CENPES*, 157 p. il.: mapa.
- 874 Klemperer, S. L., Hauge, T. A., Hauser, E. C., Oliver, J. E., Potter, C. J. (1986). The Moho in  
875 the northern Basin and Range province, Nevada, along the COCORP 40 N seismic-reflection  
876 transect. *Geological Society of America Bulletin*, 97(5), 603-618.
- 877 Korenaga, J., Holbrook, W. S., Kent, G. M., Kelemen, P. B., Detrick, R. S., Larsen, H. C.,  
878 Dahl-Jensen, T. (2000). Crustal structure of the southeast Greenland margin from joint refraction  
879 and reflection seismic tomography. *Journal of Geophysical Research: Solid Earth*, 105(B9), 21591-  
880 21614.
- 881 Lana, M. C. (1990) Bacia de Sergipe-Alagoas: Uma Hipótese de Evolução Tectono-  
882 Sedimentar. *Origem e Evolução de Bacias Sedimentares - coordenadores Raja Gabaglia, G. P. e*  
883 *Milani, E. M - Petrobras/Serec/Censud*, p.311-332.
- 884 de Lima, M. V. A., Berrocal, J., Soares, J. E., Fuck, R. A. (2015). Deep seismic refraction  
885 experiment in northeast Brazil: New constraints for Borborema province evolution. *Journal of*  
886 *South American Earth Sciences*, 58, 335-349.
- 887 Liu, Z., Bleistein, N. (1995). Migration velocity analysis: Theory and an iterative  
888 algorithm. *Geophysics*, 60(1), 142-153.
- 889 Ludwig W.J., Nafe J.E. Drake L.E. (1970). Seismic refraction. Maxwell, A.E. (Editor), *The*  
890 *Sea. New concepts of sea floor evolution*. Wiley-Interscience, New York, 4(I): 53-84.
- 891 Lutter, W. J., Nowack, R. (1990). Inversion for crustal structure using reflections from the  
892 PASSCAL Ouachita experiment. *Journal of Geophysical Research: Solid Earth*, 95(B4), 4633-  
893 4646.
- 894 Mohriak, W.U., Rabelo, J.H.L., Matos, R.D., Barros, M.C. (1995). Deep Seismic Reflection  
895 Profiling of Sedimentary Basins offshore Brazil: Geological Objectives and Preliminary Results in  
896 the Sergipe Basin. *Journal of Geodynamics*, 20:515-539
- 897 Mohriak, W.U., Bassetto, M. Vieira, I.S. (1998). Crustal Architecture and Tectonic Evolution  
898 of the Sergipe–Alagoas and Jacuípe Basins, Offshore Northeastern Brazil. *Tectonophysics*,  
899 288:199-220.
- 900 Mohriak, W.U., Mello, M.R., Bassetto, M., Vieira, I.S., Koutsoukos, E.A.M. (2000). Crustal  
901 architecture, sedimentation, and petroleum systems in the Sergipe–Alagoas Basin, Northeastern  
902 Brazil. In: Mello, M.R., Katz, B.J. (eds.). *Petroleum systems of South Atlantic margins*, AAPG  
903 *Memoir 73:273-300*
- 904 Mohriak, W. U. (2003). Bacias sedimentares da margem continental Brasileira. *Geologia,*  
905 *tectônica e recursos minerais do Brasil*, 3, 87e165.
- 906 Moulin, M., D. Aslanian, J.-L. Olivet, I. Contrucci, L. Matias, L. Géli, F. Klingelhoefer, H.  
907 Nouzé, J.-P. Réhault, and P. Unternehr (2005). Geological constraints on the evolution of the  
908 Angolan margin based on reflection and refraction seismic data (ZaiAngo project). *Geophysical*  
909 *Journal International*, 162(3), 793-810.
- 910 Moulin, M., D. Aslanian, and P. Unternehr (2010), (2010). A new starting point for the South  
911 and Equatorial Atlantic Ocean. *Earth-Science Reviews*, 98(1-2), 1-37.

- 912 Oliveira, D.C., Windley, B.F., Araújo, D.B. (2010). The Neoproterozoic Sergipano orogenic  
913 belt, NE Brazil: A complete plate tectonic cycle in western Gondwana. *Precambrian Research* 181,  
914 64-84.
- 915 Oliveira, R. G. D. (2008). Arcabouço geofísico, isostasia e causas do magmatismo cenozóico  
916 da Província Borborema e de sua margem continental (Nordeste do Brasil).
- 917 Pavlis, N. K., Holmes, S. A., Kenyon, S. C., Factor, J. K. (2012). The development and  
918 evaluation of the Earth Gravitational Model 2008 (EGM2008). *Journal of Geophysical Research:*  
919 *Solid Earth*, 117(B4).
- 920 Sandwell, D. T., Müller, R. D., Smith, W. H., Garcia, E., Francis, R. (2014). New global  
921 marine gravity model from CryoSat-2 and Jason-1 reveals buried tectonic  
922 structure. *Science*, 346(6205), 65-67.
- 923 Sandwell, D., Smith, W. (1997). Marine gravity anomaly from GEOSAT and ERS-1 satellite  
924 altimetry. *Journal of Geophysical Research*, 102:10.039-10.054.
- 925 Santos, E. D., Silva Filho, M. A. (1975). Ensaio interpretativo sobre as evolução da  
926 Geossinclinal de Propriá, Nordeste do Brasil. *Revista Mineração e Metalurgia*, 367, 3-22.
- 927 Schaller, H. (1970). Revisão estratigráfica da bacia Sergipe-Alagoas. Boletim Técnico da  
928 Petrobrás. 12 (1): 21-86
- 929 Skolotnev S. G., Bylinskaya M. E, Golovina L. A., and Ipat'eva I. S. (2012). The Origin of  
930 Bahia Seamounts (Brazil Basin, South Atlantic) in Connection to New Data on Their Age. *Doklady*  
931 *Earth Sciences*, 2012, Vol. 443, Part 2, pp. 444–450. ISSN 1028\_334X.
- 932 Silva Filho, M. A., (1998). Arco vulcânico Canindé-Marancó e a Faixa Sul-Alagoana:  
933 sequências orogênicas Mesoproterozóicas. In: *XL Congresso Brasileiro de Geologia, Belo*  
934 *horizonte, SBG*. p. 16.
- 935 Soares J.E.P., Berrocal J., Fuck R.A., Mooney W.D. Ventura D.B.R. (2006). Seismic  
936 characteristics of central Brazil crust and upper mantle: A deep seismic refraction study. *Journal of*  
937 *Geophysical Research*, 111: 1-31.
- 938 Soares, J. E. P., de Lima, M. V., Fuck, R. A., Berrocal, J. (2010). Características sísmicas da  
939 litosfera da Província Borborema: Resultados parciais do experimento de refração sísmica profunda.  
940 In *IV Simpósio Brasileiro de Geofísica*.
- 941 Stockwell, J. W., Jr. (1999), The CWP/SU: Seismic Unix package, *Comput. Geosci.*, 25(4),  
942 415–419, doi:10.1016/S0098-3004(98)00145-9.
- 943 Szatmari, P. (1998). Tectonic habitat of petroleum along the South Atlantic margins. In *Am.*  
944 *Assoc. Petrol. Geol. International Conference Extended Abstracts Volume, Rio de Janeiro, Brazil*,  
945 pp. 362±363.
- 946 Szatmari, P., Milani, E.J. (1999). Microplate rotation in northeast Brazil during South Atlantic  
947 rifting: analogies with the Sinai microplate. *Geology*, 27(12):1115-1118
- 948 Tard F., Masse P., Walgenwitz F., Gruneisen P., The volcanic passive margin in the vicinity  
949 of Aden, Yemen, *Bulletin des centres de recherche et d'exploration-production Elf-Aquitaine* 15  
950 (1991) 1–9
- 951 Tavares, E. J., Soares, J. E. P., Fuck, R. A., De Lima, M. V. A. (2012). Modelagem de onda P  
952 e razão Vp/Vs da crosta sob a linha de refração sísmica profunda NW-SE da Província Borborema.  
953 In *V Simpósio Brasileiro de Geofísica*.
- 954 White, R. S., McKenzie, D. and O'Nions, R. K. (1992). Oceanic crustal thickness from  
955 seismic measurements and rare earth element inversions. *Journal of Geophysical Research: Solid*  
956 *Earth*, 97(B13), 19683-19715. doi:10.1029/92JB01749.

957 Zelt, C. A. (1999), Modelling strategies and model assessment for wide angle seismic  
958 traveltimes data, *Geophysical Journal International*, 139, 183–204.

959

960

961

962

963

964

965

966

967

968

969

970

971

972

973

ACCEPTED MANUSCRIPT